The inner structure of ΛCDM haloes – II. Halo mass profiles and low surface brightness galaxy rotation curves

E. Hayashi,[1]★ J. F. Navarro,[1] C. Power,[2] A. Jenkins,[2] C. S. Frenk,[2] S. D. M. White,[3] V. Springel,[3] J. Stadel[4] and T. R. Quinn[5]

[1]*Department of Physics and Astronomy, University of Victoria, Victoria, BC, V8P 1A1, Canada*
[2]*Institute for Computational Cosmology, Department of Physics, University of Durham, South Road, Durham DH1 3LE*
[3]*Max-Planck Institute for Astrophysics, Garching, Munich, D-85740, Germany*
[4]*Institute for Theoretical Physics, University of Zurich, Zurich CH-8057, Switzerland*
[5]*Department of Astronomy, University of Washington, Seattle, WA 98195, USA*

ABSTRACT

We use a set of high-resolution cosmological N-body simulations to investigate the inner mass profile of galaxy-sized cold dark matter (CDM) haloes. These simulations extend the numerical convergence study presented in Paper I of this series, and demonstrate that the mass profile of CDM galaxy haloes can be robustly estimated beyond a minimum converged radius of order $r_{conv} \sim 1\,h^{-1}$ kpc in our highest-resolution runs. The density profiles of simulated haloes become progressively shallower from the virial radius inwards, and show no sign of approaching a well-defined power law near the centre. At r_{conv}, the density profile is steeper than expected from the formula proposed by Navarro, Frenk & White, which has a $\rho \propto r^{-1}$ cusp, but significantly shallower than the steeply divergent $\rho \propto r^{-1.5}$ cusp proposed by Moore et al. We perform a direct comparison of the spherically averaged dark matter circular velocity profiles with Hα rotation curves of a sample of low surface brightness (LSB) galaxies. We find that most galaxies in the sample (about 70 per cent) have rotation curves that are consistent with the structure of CDM haloes. Of the remainder, 20 per cent have rotation curves which cannot be fit by any smooth fitting function with few free parameters, and 10 per cent are inconsistent with CDM haloes. However, the latter consist mostly of rotation curves that do not extend to large enough radii to accurately determine their shapes and maximum velocities. We conclude that the inner structure of CDM haloes is not manifestly inconsistent with the rotation curves of LSB galaxies.

Key words: galaxies: formation – galaxies: kinematics and dynamics – galaxies: spiral – cosmology: theory – dark matter.

1 INTRODUCTION

The structure of dark matter haloes and its relation to the cosmological context of their formation have been studied extensively over the past few decades. Early analytical calculations focused on the scale-free nature of the gravitational accretion process and suggested that halo density profiles might be simple power laws (Gunn & Gott 1972; Fillmore & Goldreich 1984; Hoffman & Shaham 1985; White & Zaritsky 1992). Cosmological N-body simulations, however, failed to confirm these analytical expectations. Although power laws with slopes close to those motivated by the theory were able to describe some parts of the halo density profiles, even early

simulations found significant deviations from a single power law in most cases (Frenk et al. 1985, 1988; Quinn, Salmon & Zurek 1986; Dubinski & Carlberg 1991; Crone, Evrard & Richstone 1994). More systematic simulation work concluded that power-law fits were inappropriate, and that, properly scaled, dark haloes spanning a wide range in mass and size are well fit by a 'universal' density profile (Navarro, Frenk & White 1995, 1996, 1997, hereafter NFW):

$$\rho_{NFW}(r) = \frac{\rho_s}{(r/r_s)(1 + r/r_s)^2}. \tag{1}$$

One characteristic feature of this fitting formula is that the logarithmic slope, $\beta(r) = -\mathrm{d}\log\rho/\mathrm{d}\log r = (1 + 3\,r/r_s)/(1 + r/r_s)$, increases monotonically from the centre outwards. The density profile steepens with increasing radius; it is shallower than isothermal inside the characteristic scale radius r_s, and steeper than isothermal for $r > r_s$. Another important feature illustrated by this fitting

★E-mail: ehayashi@uvic.ca

formula is that the profiles are 'cuspy' [$\beta_0 = \beta(r = 0) > 0$]: the dark matter density (but not the potential) diverges at small radii.

Subsequent work has generally confirmed these trends, but has also highlighted potentially important deviations from the NFW fitting formula. In particular, Fukushige & Makino (1997, 2001) and Moore and collaborators (Moore et al. 1998, 1999, hereafter M99; Ghigna et al. 2000) have reported that NFW fits to their simulated haloes (which had much higher mass and spatial resolution than the original NFW work) underestimate the dark matter density in the innermost regions ($r < r_s$). These authors proposed that the disagreement was indicative of inner density 'cusps' steeper than the NFW profile and advocated a simple modification to the NFW formula with $\beta_0 = 1.5$ (rather than 1.0).

The actual value of the asymptotic slope, β_0, is still being hotly debated in the literature [Jing et al. 1995; Klypin et al. 2001; Taylor & Navarro 2001; Navarro 2003; Power et al. 2003 (Paper I in this series, hereafter referred to as P03); Fukushige, Kawai & Makino 2004], but there is general consensus that cold dark matter (CDM) haloes are indeed cuspy. This has been recognized as an important result, because the rotation curves of many disc galaxies, and in particular of low surface brightness (LSB) systems, appear to indicate the presence of an extended region of constant dark matter density: a dark matter 'core' (Flores & Primack 1994; Moore 1994; Burkert 1995; Blais-Ouellette, Amram & Carignan 2001; de Blok et al. 2001a; de Blok, McGaugh & Rubin 2001b).

Unfortunately, rotation curve constraints are strongest just where numerical simulations are least reliable. Resolving CDM haloes down to the kpc scales probed by the innermost points of observed rotation curves requires extremely high mass and force resolution, as well as careful integration of particle orbits in the central, high-density regions of haloes. This poses a significant computational challenge that has been met in very few of the simulations published to date.

This difficulty has meant that rotation curves have usually been compared with extrapolations of the simulation data into regions that may be severely compromised by numerical artefact. Such extrapolations rely heavily on the (untested) applicability of the fitting formula used. This practice does not allow for halo-to-halo variations, temporary departures from equilibrium or deviations from axisymmetry to be taken into account when modelling the observational data.

Finally, the theoretical debate on the asymptotic central slope of the dark matter density profile, β_0, has led at times to unwarranted emphasis on the innermost regions of rotation curves, rather than on an appraisal of the data over the full radial extent. For example, de Blok et al. (2001a,b) derive constraints on β_0 from the innermost few points of their rotation curves, and conclude that $\beta_0 \sim 0$ for most galaxies in their sample. However, this analysis focuses on the regions most severely affected by non-circular motions, seeing, misalignments and slit offsets. Such effects limit the accuracy of circular velocity estimates based on long-slit spectra. It is perhaps not surprising, then, that other studies have disputed the conclusiveness of these findings. For example, an independent analysis of data of similar quality by Swaters et al. (2003, hereafter S03) – see also van den Bosch et al. (2000) – concludes that the data are consistent with both cuspy ($\beta_0 \simeq 1$) and cored ($\beta_0 \simeq 0$) dark matter haloes. This issue is further complicated by recent simulation data (P03) which show scant evidence for a well-defined value of β_0 in CDM haloes. Given these difficulties, focusing the theoretical or observational analysis on β_0 does not seem promising.

In this paper, we improve upon previous work by comparing circular velocity curves from simulations directly with the full measured rotation curves of LSB galaxies. We present results from a set of seven galaxy-sized dark matter haloes, each of which has been simulated at various resolution levels in order to ascertain the numerical convergence of our results. This allows us to test rigorously the P03 convergence criteria, as well as to clarify the cusp–core discrepancy through direct comparison between observation and simulation. A companion paper (Navarro et al. 2004) addresses the issue of universality of CDM halo structure using simulations that span a wide range of scales, from dwarf galaxies to galaxy clusters.

The outline of this paper is as follows. In Section 2 we introduce our set of simulations and summarize briefly our numerical methods. The seven galaxy-sized haloes that form the core of our sample have been simulated at various resolutions, and we use them in Section 3 to investigate the robustness of the P03 numerical convergence criteria. The density profiles of these haloes are presented and compared with previous work in Section 4. In Section 5 we compare the halo V_c profiles with the LSB rotation curve data sets of McGaugh, Rubin & de Blok (2001, hereafter M01), de Blok & Bosma (2002, hereafter B02) and S03. Our main conclusions and plans for future work are summarized in Section 6.

2 NUMERICAL SIMULATIONS

We have focused our analysis on seven galaxy-sized dark matter haloes selected at random from two different cosmological N-body simulations of periodic boxes with comoving size $L_{box} = 32.5$ and $35.325 \, h^{-1}$ Mpc, respectively. Each of these 'parent' simulations has $N_{box} = 128^3$ particles, and adopts the currently favoured 'concordance' ΛCDM model, with $\Omega_0 = 0.3$, $\Omega_\Lambda = 0.7$, and either $h = 0.65$ (runs labelled G1, G2 and G3) or $h = 0.7$ (G4, G5, G6 and G7; see Table 1). The power spectrum in both simulations is normalized so that the linear rms amplitude of fluctuations on spheres of radius $8 \, h^{-1}$ Mpc is $\sigma_8 = 0.9$ at $z = 0$.

All haloes (G1–G7) have been resimulated at three or four different mass resolution levels; each level increases the number of particles in the halo by a factor of 8, so that the mass per particle has been varied by a factor of 512 in runs G1–G3, and by a factor of 64 in runs G4–G7 (see Table 1). All of these runs focus numerical resources on the Lagrangian region from where each system draws its mass, whilst approximating the tidal field of the whole box by combining distant particles into groups of particles whose mass increases with distance from the halo. This resimulation technique follows closely that described in detail in P03 and in Navarro et al. (2004), where the reader can find full details. For completeness, we present here a brief account of the procedure.

Haloes selected for resimulation are identified at $z = 0$ from the full list of haloes with circular velocities in the range (150, 250) km s^{-1} in the parent simulations. All particles within a sphere of radius $3 \, r_{200}$[1] centred on each halo are then traced back to the initial redshift configuration ($z_i = 49$). The region defined by these particles is typically fully contained within a box of size $L_{sbox} \simeq 5 \, h^{-1}$ Mpc, which is loaded with $N_{sbox} = 32^3$, 64^3, 128^3 or 256^3 particles. Particles in this new high-resolution region are perturbed with the same waves as in the parent simulation as well as with additional smaller scale waves up to the Nyquist frequency of the high-resolution particle grid. Particles which do not end up within $3 \, r_{200}$ of the selected halo

---

[1] We define the 'virial radius', r_{200}, as the radius of a sphere of mean density 200 times the critical value for closure, $\rho_{crit} = 3 \, H^2/8\pi G$, where H is Hubble constant. We parametrize the present value of the Hubble constant H by $H_0 = 100 \, h$ km s^{-1} kpc^{-1}.

Table 1. Numerical and physical properties of simulated haloes.

Label	R_{200} h^{-1} kpc	M_{200} $10^{10}\,h^{-1}\,M_\odot$	N_{200}	ϵ h^{-1} kpc	$N_{\Delta t}$	Code	r_{conv} h^{-1} kpc
G1/32³	202.1	191.8	5758	10	800	PKDGRAV	22.9
G1/64³	205.2	201.1	48 318	2.5	1600	PKDGRAV	7.7
G1/128³	205.1	200.6	383 560	1.25	3200	PKDGRAV	3.2
G1/256³	214.4	229.4	3 447 447	0.15625	RHOSGACC	GADGET	1.4
G2/32³	231.4	288.1	8583	10	800	PKDGRAV	24.2
G2/64³	231.8	289.8	69 088	3.5	1600	PKDGRAV	7.0
G2/128³	234.1	298.6	566 456	1.25	3200	PKDGRAV	2.9
G2/256³	232.6	292.9	4 523 986	0.5	6400	PKDGRAV	1.3
G3/32³	218.7	243.1	5484	10	800	PKDGRAV	22.5
G3/64³	215.0	231.1	41 719	3.5	1600	PKDGRAV	9.3
G3/128³	214.5	229.7	331 314	1.25	3200	PKDGRAV	3.9
G3/256³	212.7	223.8	2 661 091	0.45	6400	PKDGRAV	1.7
G4/64³	164.9	104.4	53 331	2.5	3200	PKDGRAV	5.7
G4/128³	165.4	105.3	432 313	1	6400	PKDGRAV	2.4
G4/256³	164.0	102.6	3 456 221	0.3	12800	PKDGRAV	1.0
G5/64³	165.3	105.0	62 066	3	800	PKDGRAV	5.7
G5/128³	165.7	105.8	496 720	1	3200	PKDGRAV	2.3
G5/256³	165.0	104.5	3 913 956	0.35	6400	PKDGRAV	1.0
G6/64³	160.7	96.5	57 008	3	800	PKDGRAV	6.0
G6/128³	163.2	101.1	474 844	1	3200	PKDGRAV	2.5
G6/256³	162.5	99.9	3 739 913	0.35	6400	PKDGRAV	1.0
G7/64³	159.7	94.7	55 947	3	800	PKDGRAV	5.8
G7/128³	160.9	96.9	454 936	1	3200	PKDGRAV	2.4
G7/256³	160.3	95.8	3 585 676	0.35	6400	PKDGRAV	1.0
D1	32.3	0.8	784 980	0.0625	EPSACC	GADGET	0.3
D2	34.1	0.9	778 097	0.0625	EPSACC	GADGET	0.4
D3	32.3	0.8	946 421	0.0625	EPSACC	GADGET	0.3
D4	34.7	1.0	1 002 098	0.0625	EPSACC	GADGET	0.3
C1	1502.1	78842.4	1 565 576	5.0	EPSACC	GADGET	16.8
C2	1468.1	73618.2	1 461 017	5.0	EPSACC	GADGET	16.9
C3	1300.6	51179.5	1 011 918	5.0	EPSACC	GADGET	16.1
C4	1316.7	53101.9	1 050 402	5.0	EPSACC	GADGET	15.9
C5	1375.5	60541.8	1 199 299	5.0	EPSACC	GADGET	16.2
C6	1521.1	81870.6	1 626 161	5.0	EPSACC	GADGET	15.5
C7	1245.8	44979.4	887 837	5.0	EPSACC	GADGET	16.4
C8	1365.4	59220.3	1 172 850	5.0	EPSACC	GADGET	16.8

at $z = 0$ are replaced by lower-resolution particles which replicate the tidal field acting on the high-resolution particles. This resampling includes some particles within the boundaries of the high-resolution box, and therefore the high-resolution region defines an asymmetrical 'amoeba-shaped' three-dimensional volume surrounded by tidal particles whose mass increases with distance from this region.

A summary of the numerical parameters and halo properties is given in Table 1. This table also includes reference to 12 further runs, four of them corresponding to dwarf galaxy-sized haloes and eight of them to galaxy cluster-sized haloes. These systems have been simulated only at the highest resolution ($N_{sbox} = 256^3$), and therefore are not included in our convergence analysis. These runs are discussed in detail in a companion paper (Navarro et al. 2004).

Some simulations were performed with a fixed number of time-steps for all particles using the parallel N-body code PKDGRAV of Stadel and Quinn (Stadel 2001), while others used the N-body code

GADGET (Springel, Yoshida & White 2001). The GADGET runs allowed for individual time-steps for each particle assigned using either the RHOSGACC or EPSACC criteria (see P03 for full details). The halo labelled G1 in this paper is the same one selected for the numerical convergence study presented in P03. Although PKDGRAV also has individual time-stepping capabilities, we have chosen not to take advantage of these for the simulations presented in this paper. We note that P03 find only a modest computational gain due to multistepping schemes provided that the softening parameter is properly chosen.

The softening parameter (fixed in comoving coordinates) for each simulation (with the exception of G1/256³; see P03) was chosen to match the 'optimal' softening suggested by P03

$$\epsilon_{opt} = \frac{4r_{200}}{N_{200}^{1/2}}, \tag{2}$$

where N_{200} is the number of particles within r_{200} at $z = 0$. This softening choice minimizes the number of time-steps required for convergent results by minimizing discreteness effects in the force calculations whilst ensuring adequate force resolution.

At $z = 0$, the mass within the virial radius, M_{200}, of our galaxy-sized haloes ranges from $\sim 10^{12} h^{-1} M_\odot$ to $\sim 3 \times 10^{12} h^{-1} M_\odot$, corresponding to circular velocities, $V_{200} = (GM_{200}/r_{200})^{1/2}$, in the range 160–230 km s^{-1}.

3 NUMERICAL CONVERGENCE

3.1 Criteria

P03 propose three different conditions that should be satisfied in order to ensure convergence in the circular velocity profile. According to these criteria, convergence to better than 10 per cent in the spherically averaged circular velocity, $V_c(r)$, is achieved at radii which satisfy the following conditions.

(i) The local circular orbit period $t_{circ}(r)$ is much greater than the size of the time-step Δt

$$\frac{t_{circ}(r)}{t_{circ}(r_{200})} \gtrsim 15 \left(\frac{\Delta t}{t_0} \right)^{5/6}, \tag{3}$$

where t_0 denotes the age of the Universe, which is by definition of the order of the circular orbit time-scale at the virial radius, $t_{circ}(r_{200})$.

(ii) Accelerations do not exceed a characteristic acceleration, a_ϵ, determined by V_{200} and the softening length ϵ

$$a(r) = \frac{V_c^2(r)}{r} \lesssim a_\epsilon = 0.5 \frac{V_{200}^2}{\epsilon}, \tag{4}$$

where $a(r)$ is the mean radial acceleration experienced by particles at a distance r from the centre of the system, $a(r) = GM(r)/r^2 = V_c^2(r)/r$.

(iii) Enough particles are enclosed such that the local collisional relaxation time-scale $t_{relax}(r)$ is longer than the age of the Universe[2]

$$\frac{t_{relax}(r)}{t_{circ}(r_{200})} = \frac{\sqrt{200}}{8} \frac{N(r)}{\ln N(r)} \left[\frac{\overline{\rho}(r)}{\rho_{crit}} \right]^{-1/2} \gtrsim 1, \tag{5}$$

where $N(r)$ is the number of particles and $\overline{\rho}(r)$ is the mean density within radius r.

For 'optimal' choices of the softening and time-step, as well as for the typical number of particles in our runs, we find that criterion (iii) above is the strictest. The number of high-resolution particles thus effectively defines the 'predicted' converged radius, r_{conv}, beyond which, according to P03, circular velocities should be accurate to better than 10 per cent. We emphasize that this accuracy criterion applies to the cumulative mass profile; convergence in properties such as local density estimates, $\rho(r)$, typically extends to radii significantly smaller than r_{conv}.

3.2 Validating the convergence criteria

We assess the validity of the convergence criteria listed above by comparing the mass profile of the highest-resolution run corresponding to each halo with those obtained at lower resolution. Fig. 1 illustrates the procedure. From top to bottom, the three panels in this figure show, as a function of radius, the circular orbit time-scale, the

---

[2] We adopt a slightly more conservative criterion than P03, who require $t_{relax} \gtrsim 0.6 \, t_{circ}(r_{200})$.
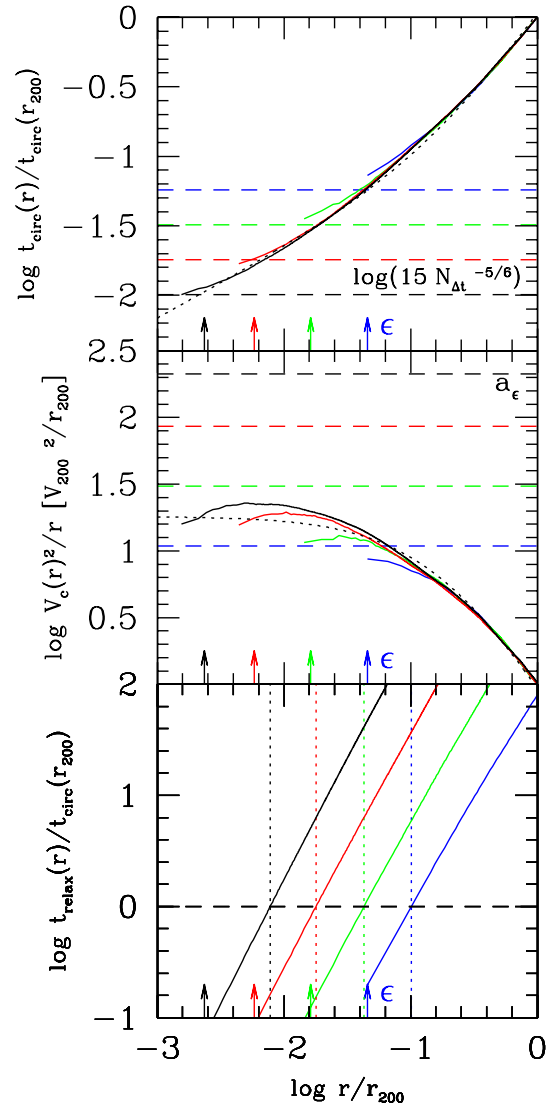
Figure 1. The structure of halo G3 at different mass, time and spatial resolutions. The value of the softening parameter ϵ is indicated by arrows in the three panels. The numbers of time-steps and particles are listed in Table 1. Runs with 32^3, 64^3, 128^3 and 256^3 high-resolution particles are shown as the solid curves from left to right, respectively. Dotted curves show an NFW profile with concentration $c = 5.3$ and $r_{200} = 143.4 \, h^{-1}$ kpc. Upper panel: local circular orbit period t_{circ} versus radius; radii at which the circular orbital time-scale is less than $15 \, N_{\Delta t}^{-5/6}$, indicated by the dashed lines for each simulation, are unresolved due to insufficient time resolution. Middle panel: mean radial acceleration profile $V_c(r)^2/r$; untrustworthy radii are those corresponding to accelerations greater than the limiting acceleration imposed by the softening $a_\epsilon \simeq 0.5 \, V_{200}^2/\epsilon$, shown by the dashed lines. Lower panel: collisional relaxation time t_{relax} versus radius; convergence requires $t_{relax} \gtrsim t_{circ}(r_{200})$. Vertical dotted lines indicate the radius, r_{conv}, beyond which this condition (the strictest of the three) is satisfied.

mean radial acceleration and the relaxation time-scale, respectively, for the four runs corresponding to halo G3. The small arrows at the bottom of each panel indicate the choice of gravitational softening for each run. The dotted curves in the top and middle panels show the best-fitting NFW profile to the converged region of the highest-resolution $N_{sbox} = 256^3$ run.

The 'converged radius' corresponding to each criterion is determined by the intersection of the horizontal dashed lines in each

panel with the 'true' profile, which we shall take to be that of the highest-resolution run (shown in solid black in Fig. 1). Clearly, the strictest criterion is that imposed by the relaxation time-scale (the dotted vertical lines in the lower panel show the converged radius corresponding to this criterion). This suggests, for example, that the lowest-resolution G3 run (with $N_{sbox} = 32^3$), should start to deviate from the converged profiles roughly at $r \sim 0.1 \, r_{200}$. Indeed, this appears to be the radius at which this profile starts to 'peel off' from the highest-resolution one, as shown in the top two panels of Fig. 1. Increasing the number of high-resolution particles by a factor of 8 typically brings the converged radius inwards by a factor of ~ 2.4. For the medium-resolution run ($N_{sbox} = 64^3$, shown in solid green), r_{conv} is predicted to be $\sim 0.04 \, r_{200}$, which again coincides well with the radius inside which departures from the converged profile are apparent. Similarly, $r_{conv} \sim 0.017 \, r_{200}$ for the high-resolution ($N_{sbox} = 128^3$) run (shown in red).

The density and circular velocity profiles corresponding to the four G3 runs are shown in Fig. 2. Panels on the left show the profiles down to the radius that contains 50 particles, whereas those on the right show the profiles restricted to $r \gtrsim r_{conv}$. Fig. 2 illustrates two important results alluded to above: (i) both $\rho(r)$ and $V_c(r)$ converge well at $r \gtrsim r_{conv}$; (ii) convergence in $\rho(r)$ extends to radii smaller than r_{conv}. Indeed, the top-left panel shows that our choice of r_{conv} is rather

conservative when applied to the density profile. Typically, densities are estimated to better than 10 per cent down to $r \sim 0.6 \, r_{conv}$.

How general are these results? Fig. 3 compares the minimum 'converged' radius predicted by the P03 criteria, r_{conv}, with $r_{10 \, per \, cent \, vc}$, the actual radius where circular velocities in the lower-resolution runs deviate from the highest-resolution run by more than 10 per cent. In essentially all cases, $r_{conv} \lesssim r_{10 \, per \, cent \, vc}$, indicating that the P03 criteria are appropriate, albeit at times somewhat conservative. We list our r_{conv} estimates for all runs in Table 1.

We note that Stoehr et al. (2003) find similar results for their Milky Way (MW) sized galaxy halo resimulated at four different levels of resolution. For example, they find that the V_c profiles for versions of their halo with $N_{200} = 1.4 \times 10^4$ and 1.3×10^5 converge to within 5 per cent of the high-resolution profile at about 6.3 and $3.5 \, h^{-1}$ kpc, respectively. For our halo G1, we find $r_{10 \, per \, cent \, vc} = 5.1$ and $1.3 \, h^{-1}$ kpc for simulations with $N_{200} = 4.8 \times 10^4$ and 3.8×10^5, respectively.

4 HALO STRUCTURE AND FITTING FORMULAE

The dotted curves in Fig. 2 show the best NFW fits to the density and circular velocity profile of the highest-resolution run. The dashed
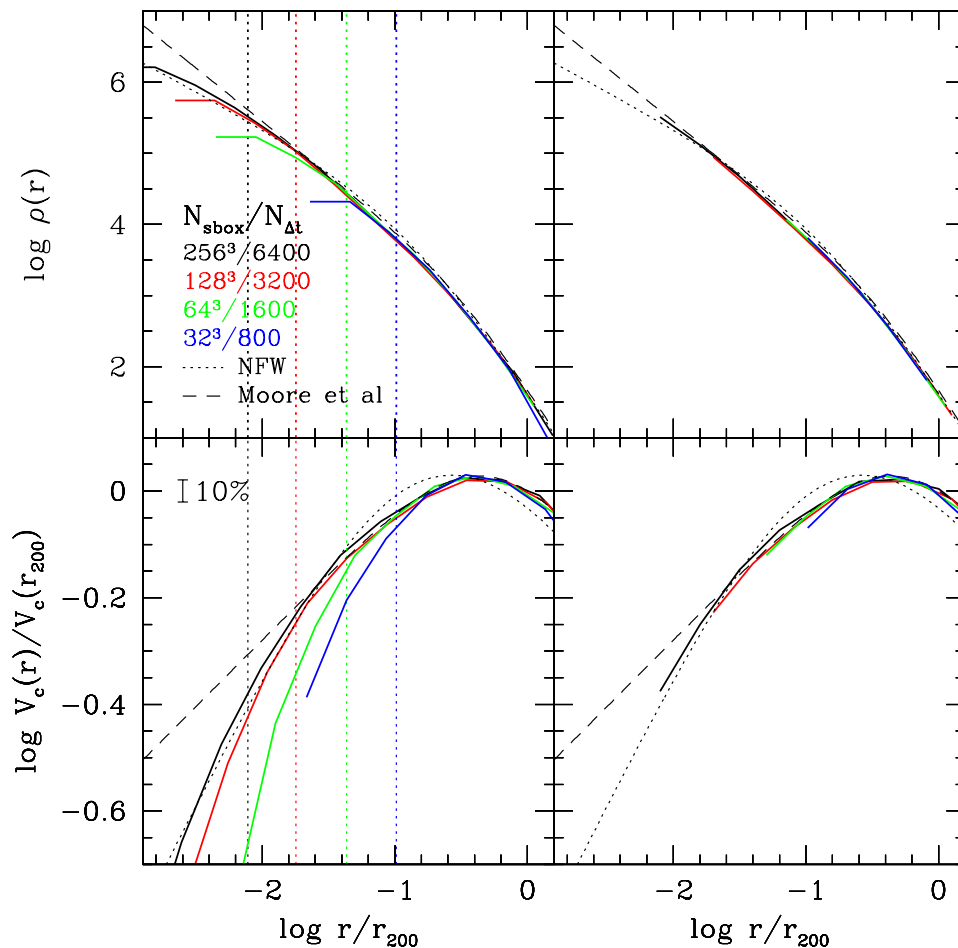

Figure 2. Upper-left panel: density profiles of halo G3 at four different levels of mass resolution, plotted down to radii containing 50 particles. Dashed and dotted curves show best-fitting M99 and NFW profiles, respectively (see text for fitting details). Vertical dotted lines indicate the minimum converged radius, r_{conv}, for each run. Upper-right panel: same density profiles plotted only for converged radii. The discrepancy between lower-resolution runs and the highest-resolution simulation at small radii is no longer apparent when only reliably resolved radii are considered. Lower panels are as the upper ones, but for the circular velocity profiles.
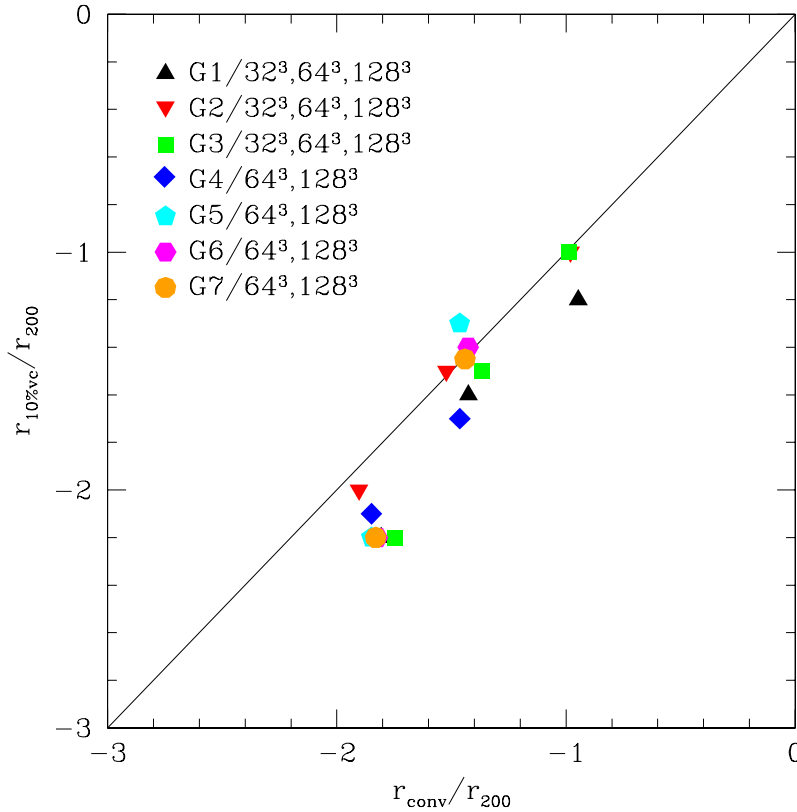
Figure 3. Radius where the circular velocity profile of lower-resolution runs starts to deviate from that of the highest-resolution run by more than 10 per cent, $r_{10\,per\,cent\,vc}$, plotted against the minimum converged radius predicted by the P03 convergence criteria, r_{conv}. In all cases $r_{conv} \leqslant r_{10\,per\,cent\,vc}$, validating the P03 criteria as conservative estimators of the converged region.

lines correspond to the best fit adopting the modification to the NFW profile advocated by M99:

$$\rho_{Moore}(r) = \frac{\rho_M}{(r/r_M)^{1.5}\left(1 + (r/r_M)^{1.5}\right)}. \tag{6}$$

These fits are obtained by straightforward χ^2 minimization in two parameters, r_s or r_M, and the characteristic density, ρ_s or ρ_M. The profiles are calculated in bins of equal width in $\log r$, and the fits are performed over the radial range $r_{conv} < r < r_{200}$. Equal weights are assigned to each radial bin because the statistical (Poisson) uncertainty in the determination of the mass within each bin is negligible (each bin contains thousands of particles) so uncertainties are completely dominated by systematic errors whose radial dependence is difficult to assess quantitatively.

The best fits to $\rho(r)$ and $V_c(r)$ shown in Fig. 2 are obtained independently from each other. Values of the concentration parameter, $c_{NFW} = r_{200}/r_s$, for the best-fitting NFW profiles are 6.4 and 5.3 for fits to the density and circular velocity profile, respectively. The M99 concentrations, $c_{Moore} = r_{200}/r_M$, are 3.0 and 2.9 for the best fits to $\rho(r)$ and $V_c(r)$, respectively. Over the converged region, $r \gtrsim r_{conv}$, both the NFW and M99 profiles appear to reproduce reasonably well the numerical simulation results. Indeed, no profile in the G3 runs deviates by more than 10 per cent in V_c or 30 per cent in $\rho(r)$ from the best fits obtained with either equation (1) or equation (6). More substantial differences are expected only well inside r_{conv}, but these regions are not reliably probed by the simulations. This suggests that either the NFW profile or M99 profile may be used to describe the structure of ΛCDM haloes outside $\sim$1 per cent

of the virial radius, but it also implies that one should be extremely wary of extrapolations inside this radius.

4.1 Radial dependence of the logarithmic slope

One intriguing feature of Fig. 2 is that the M99 formula appears to fit the G3 density profiles as well or better than that of NFW, but that V_c profiles are somewhat better approximated by NFW (see also P03). This suggests that neither formula captures fully and accurately the radial dependence of the structure of ΛCDM haloes.

This view is confirmed by the radial dependence of the logarithmic slope of the density profile $\beta(r) = -d \log \rho/d \log r$, which is shown in the top-left panel of Fig. 4 for all the high-resolution runs, and compared with the predictions of the NFW (solid line) and M99 (dashed line) formulae. Logarithmic slopes are calculated by numerical differentiation of the density profile, computed in radial bins of equal logarithmic width ($\Delta \log r/r_{200} \simeq 0.2$). The slope profiles in Fig. 4 are normalized to r_{-2}, the radius where $\beta(r)$ takes the 'isothermal' value of 2.[3] In this and all subsequent figures, profiles are shown only down to the minimum converged radius r_{conv}. This corresponds typically to a radius $r_{conv} \simeq 0.006\,r_{200}$, or about 1–$2\,h^{-1}$ kpc for haloes simulated at highest resolution (see Table 1).

The top-left panel of Fig. 4 shows that haloes differ from the NFW and M99 formula in a number of ways, as follows.

(i) There is no obvious convergence to an asymptotic value of the logarithmic slope at the centre; the profile becomes shallower

---

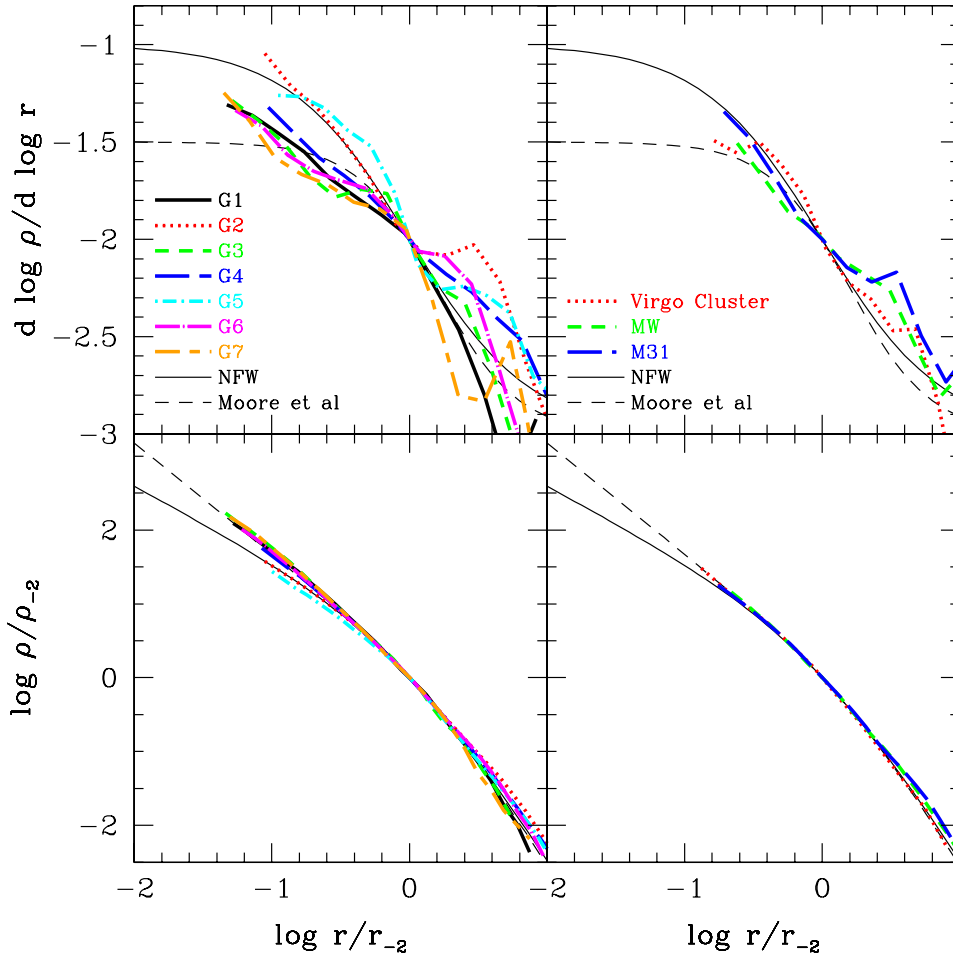[3] r_{-2} is in this sense equivalent to the scale radius r_s of the NFW profile.

Figure 4. Upper-left panel: logarithmic slope of the density profile of haloes simulated at our highest resolution $N_{sbox} = 256^3$, plotted for $r \geqslant r_{conv}$. Curves are scaled horizontally to the radius r_{-2}, where the slope takes the isothermal value, $d \log \rho / d \log r \, (r_{-2}) = -2$. NFW and M99 profiles are shown as solid and dashed curves, respectively. The logarithmic slope increases monotonically with decreasing radius and there is no obvious convergence to a particular asymptotic value of the central slope. Upper-right panel: same as upper-left panel but for the SCDM Virgo cluster of Ghigna et al. (2000) and SCDM MW and M31 galaxy haloes of M99. The profiles of the two galaxy-sized haloes appear to be consistent with those of our haloes. The logarithmic slope of the cluster halo appears to be slightly steeper than the others, fluctuating about a value of -1.4 at the innermost resolved point. Lower-left panel: halo density profiles scaled horizontally to radius r_{-2} and vertically to the corresponding density at that radius $\rho_{-2} \equiv \rho(r_{-2})$. Lower-right panel: same as lower-left panel but for the Ghigna et al. (2000) and M99 haloes.

all the way down to the innermost radius reliably resolved in our runs, r_{conv}.

(ii) The slope at r_{conv} is significantly shallower than the asymptotic value of $\beta_0 = 1.5$ advocated by M99. The shallowest value measured at r_{conv} is $\beta \simeq 1$, and the average over all seven haloes is $\beta \simeq 1.2$.

(iii) Most halo profiles become shallower with radius more gradually than predicted by the NFW formula; at $r \sim 0.1 \, r_{-2}$ the average slope is ~ -1.4, whereas NFW would predict ~ -1.18. The NFW density profile turns over too sharply from $\rho \propto r^{-3}$ to $\rho \propto r^{-1}$ compared to the simulations.

In other words, the M99 profile appears to fit better the inner regions of the density profile of some ΛCDM haloes (see bottom-left panel of Fig. 4) not because the inner density cusp diverges as steeply as $\beta_0 = 1.5$, but rather because its logarithmic slope becomes shallower inwards less rapidly than NFW.

It is important to note as well that there is significant scatter from halo to halo, and that two of the seven density profiles are actually fit better by the NFW formula. Are these global deviations from a 'uni-

versal' profile due to substructure? We have addressed this question by removing substructure from all haloes and then recomputing the slopes. Substructure is removed by first computing the local density at the position of each particle, ρ_i, using a spline kernel similar to that used in smoothed particle hydrodynamics (SPH) calculations.[4] Then, we remove all particles whose densities are more than two standard deviations above the spherically averaged mean density at its location. (The mean and standard deviation are computed in bins of equal logarithmic width, $\Delta \log r/r_{200} \simeq 0.01$.) The procedure is iterated until no further particles are removed. The remaining particles form a smoothly distributed system that appears devoid of substructure on all scales. We find that density profiles are smoother after the removal of substructure but that most of the variation in the overall shapes of the profiles remains. We conclude that the presence of substructure is not directly responsible for the observed scatter in the shape of halo density profiles.

---

[4] See http://www-hpcc.astro.washington.edu/tools/smooth.html.

4.2 Comparison with other work

Are these conclusions consistent with previous work? To explore this issue, we have computed the logarithmic slope profile of three CDM haloes run by Moore and collaborators. The haloes we have reanalysed are the MW-like and M31-like galaxy haloes of the Local Group system from M99 and the LORES version of the 'Virgo' cluster halo from Ghigna et al. (2000). The $z \simeq 0.1$ output of the Local Group simulation was provided for us by the authors, whereas the Virgo cluster was rerun using initial conditions available from Moore's website.[5] The Virgo cluster run used the same *N*-body code as the original simulation (PKDGRAV) but was run with a fixed number of time-steps (12 800). A run with 6400 time-steps was also carried out and no differences in the mass profiles were detected. The numbers of particles within the virial radius are 1.2×10^6, 1.7×10^6 and 5.0×10^5 for the MW, M31 and LORES Virgo cluster haloes, respectively.

Fig. 4 shows the logarithmic slope (upper-right panel) and density (lower-right panel) profiles corresponding to these haloes, plotted down to the minimum converged radius r_{conv}. No major differences between these simulations and ours are obvious from these panels. It is clear, for example, that at the innermost converged point, the slope of the density profile of the two Local Group haloes is significantly shallower than $r^{-1.5}$, and shows no signs of having converged to a well-defined power-law behaviour. There is some evidence for 'convergence' to a steep cusp ($r^{-1.4}$) in the LORES Virgo cluster simulation, but the dynamic range over which this behaviour is observed is rather limited. The Virgo cluster run thus appears slightly unusual when compared with other systems in our ensemble. Although our reanalysis confirms the conclusion of Moore et al. (1998, 1999) that this particular system appears to have a steeply divergent core, this does not seem to be a general feature of ΛCDM haloes.

We also note that the highest-resolution simulation of a galaxy halo is currently the $N_{200} = 1.0 \times 10^7$ MW-sized halo of Stoehr et al. (2003). These authors estimate that the V_c profile of this halo is resolved to within 5 per cent of the converged solution down to $0.004 \, r_{200}$ or about $0.7 \, h^{-1}$ kpc and they conclude that the inner slope of the density profile of this halo is significantly shallower than $r^{-1.5}$ at radii greater than this minimum converged radius.

Our results thus lend support to the conclusions of Klypin et al. (2001), who argue that there is substantial scatter in the inner profiles of CDM haloes. Some are best described by the NFW profile whereas others are better fit by the M99 formula, implying that studies based on a single halo might reach significantly biased conclusions.

Finally, we note that deviations from either fitting formula in the radial range resolved by the simulations, although significant, are small. Best NFW/M99 fits are typically accurate to better than ∼20 per cent in circular velocity and ∼40 per cent in density, respectively. We discuss in a companion paper (Navarro et al. 2004) the constraints placed by our simulations on extrapolations of these formulae to the inner regions as well as on the true asymptotic inner slope of ΛCDM halo density profiles.

5 HALO CIRCULAR VELOCITY PROFILES AND LSB ROTATION CURVES

As discussed in Section 1, an important discrepancy between the structure of CDM haloes and the mass distribution in disc galaxies

inferred from rotation curves has been noted repeatedly in the literature over the past decade (Moore 1994; Flores & Primack 1994; Burkert 1995; McGaugh & de Blok 1998; M99; van den Bosch et al. 2000; Côté et al. 2000; Blais-Ouellette et al. 2001; van den Bosch & Swaters 2001; Jimenez et al. 2003). In particular, the shape of the rotation curves of LSB galaxies has been identified as especially difficult to reconcile with the cuspy density profiles of CDM haloes.

Given the small contribution of the baryonic component to the mass budget in these galaxies, the rotation curves of LSB discs are expected to trace rather cleanly the dark matter potential, making them ideal probes of the inner structure of dark matter haloes in LSBs. Many of these galaxies are better fit by circular velocity curves arising from density profiles with a well-defined constant density 'core' rather than the cuspy ones inferred from simulations, a result that has prompted calls for a radical revision of the CDM paradigm on small scales (see, for example, Spergel & Steinhardt 2000).

It is important, however, to note a number of caveats that apply to the LSB rotation curve problem.

(i) Many of the early rotation curves where the disagreement was noted were unduly affected by beam smearing in the H I data (Swaters, Madore & Trewhella 2000). For example, van den Bosch et al. (2000) argue that, once beam smearing is taken into account, essentially all H I LSB rotation curves are consistent with cuspy halo profiles. The observational situation has now improved substantially thanks to higher-resolution rotation curves obtained from long-slit Hα observations (see, for example, M01; de Blok et al. 2001a; Swaters et al. 2000; S03). We shall restrict our analysis to these rotation curves in what follows.

(ii) Strictly speaking, the observational disagreement is with the fitting formulae, rather than with the actual structure of simulated CDM haloes. As noted in the previous section, there are systematic differences between them, so it is important to confirm that the disagreement persists when LSB rotation curves are contrasted directly with simulations.

(iii) Finally, it must be emphasized that the rotation curve problem arises when comparing rotation speeds of gaseous discs to the spherically averaged circular velocity profiles of dark matter haloes. Given that CDM haloes are expected to be significantly nonspherical (Davis et al. 1985; Barnes & Efstathiou 1987; Warren et al. 1992; Jing et al. 1995; Thomas et al. 1998; Jing & Suto 2002), some differences between the two are to be expected. It is therefore important to use the full three-dimensional structure of CDM haloes to make predictions regarding the rotation curves of gaseous discs that may be compared directly to observation. We shall neglect this complex issue in this paper, but we plan to explore in detail the rotation curves of gaseous discs embedded in such asymmetric potentials in future papers of this series.

In what follows, we compare directly the circular velocity profiles of our simulated haloes with the observational data. This procedure has the advantage of retaining the diversity in the shapes of halo profiles that is often lost when adopting simple analytical fitting formulae. In addition, we consider circular velocity profiles only down to the innermost converged radius, thereby eliminating uncertainties about the reliability of the profile at very small radii.

We begin the analysis by emphasizing the importance of taking into account the changes in the central halo mass profile induced by accretion events. Indeed, these may trigger and sustain departures from the 'average' profile that may be detectable in the rotation curves of embedded gaseous discs. We shall then describe a simple characterization of rotation curve shapes that may be applied to

---

[5] See http://www.nbody.net. We note that all of these runs were evolved in a standard CDM (SCDM) $\Omega_0 = 1$ cosmogony, rather than the ΛCDM scenario we adopt in this paper.

both observational and simulation data. This enables a direct and quantitative assessment of the 'cusp' versus 'core' problem as it applies to the most recent LSB data sets.

5.1 Evolution of the inner mass profile

Systematic – and at times substantial – changes in the inner circular velocity profile are induced by accretion events during the assembly of the halo, even when such events might contribute only a small fraction of mass to the inner regions. These transients may increase substantially the scatter in the shape of the V_c profiles and they ought to be taken into account when comparing with observation.

This is illustrated in Fig. 5, which shows the evolution of the mass and circular velocity profiles of halo G1. The top panel of this figure shows the evolution of the mass enclosed within 2, 10 and 20 kpc (physical), and r_{200}, as a function of redshift. Although the mass
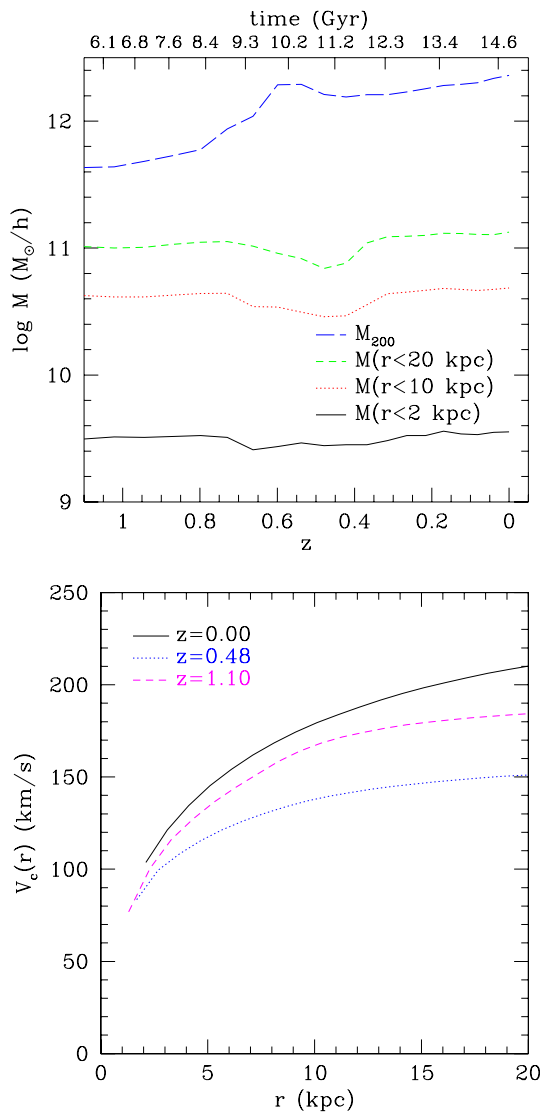

Figure 5. Top panel: mass within $r = 2$, 10 and 20 kpc (physical) and r_{200} for halo G1/256^3 as a function of redshift (age of Universe in Gyr) on bottom (top) axis. The mass within 20 kpc undergoes significant fluctuations in response to a merger at $z \simeq 0.7$. Bottom panel: the inner circular velocity profile before ($z = 1.10$), during ($z = 0.48$) and after ($z = 0$) the merger. The shape of the V_c profile is noticeably altered by the effects of the infalling substructure.

inside 20 kpc increases by less than $\sim$25 per cent because $z = 1$, there are significant ($\sim$50–60 per cent) fluctuations during this time caused by the tidal effects of orbiting substructure and accretion events. Most noticeable is a major merger at $z \simeq 0.7$, which affects the mass profile down to the innermost reliably resolved radius, $\simeq$2 kpc.

The effect of these fluctuations on the circular velocity profile is shown in the bottom panel of Fig. 5. Here we show the inner 20 kpc of the circular velocity profile before ($z = 1.1$), during ($z = 0.48$) and after ($z = 0$) a major accretion event. Substantial changes in the shape of the V_c profile are evident as the halo responds to the infalling substructure. Note that the changes persist over time-scales of the order of $\gtrsim$1 Gyr, exceeding the circular orbital period at $r = 2$, 10 and 20 kpc ($\sim$0.13, 0.34 and 0.58 Gyr, respectively). These relatively long-lasting changes thus would likely be reflected in the dynamics of a disc present at the centre of the halo.

5.2 LSB rotation curve shapes

Could the evolutionary effects discussed above be responsible, at least in part, for the constant density cores inferred from the rotation curves of LSB and dwarf galaxies? Because it is nearly impossible to tailor a simulation to reproduce individual galaxies in detail, it is important to adopt a simple characterization of the rotation curves that allows for a statistical assessment of the disagreement between halo V_c profiles and observation. We have thus adopted a three-parameter fitting formula commonly used in observational work to describe optical rotation curves (Courteau 1997):

$$V(r) = \frac{V_0}{(1 + x^\gamma)^{1/\gamma}}. \qquad (7)$$

Here V_0 is the asymptotic velocity, $x = r_t/r$, where r_t is a scale radius, and the dimensionless parameter γ describes the overall shape of the curve. The larger the value of γ the sharper the turnover from the "rising" to the "flat" region of the velocity curve. Equation (7) is flexible enough to accommodate the shape of essentially all rotation curves in the samples we consider here. We note that this formula has three free parameters,[6] one more than the NFW profile. This fitting formula is plotted for several different combinations of parameters in Fig. 6 alongside NFW and pseudo-isothermal V_c profiles.[7] The left panel shows that equation (7) can accurately reproduce both NFW and pseudo-isothermal profiles, despite the fact that the logarithmic slopes of these profiles tend to different values at small radii, 0.5 and 1, respectively, as shown in the right panel of this figure. This figure also illustrates the difference between fits with different values of γ. Fits with $\gamma \gg 1$ rise linearly with radius out to $r \simeq r_t$ then quickly turn over, becoming flat at $r \gtrsim r_t$. Fits with lower γ have a much more gradual transition between the $V \propto r$ and $V \simeq$ constant parts of the velocity curve.

We have applied this fitting formula to the Hα rotation curve data sets of M01,[8] B02,[9] and S03.[10] The M01 sample consists of 26 LSB

---

[6] An additional factor of $(1 + x)^\beta$ was used by Courteau (1997) to improve fits to $\sim$10 per cent of the galaxies in his sample that exhibit a drop-off in the outer part of the rotation curve. For simplicity, we have not included this parameter in our fits.

[7] The density profile of this widely used approximation to the non-singular isothermal sphere is given by $\rho_{\mathrm{iso}}(r) = \rho_0/[1 + (r/r_c)^2]$, where r_c is the radius of a constant density core and ρ_0 is the characteristic density of the core.

[8] See http://www.astro.umd.edu/~ssm/data.

[9] See ftp://cdsarc.u-strasbg.fr/cats/J/A+A/385/816.
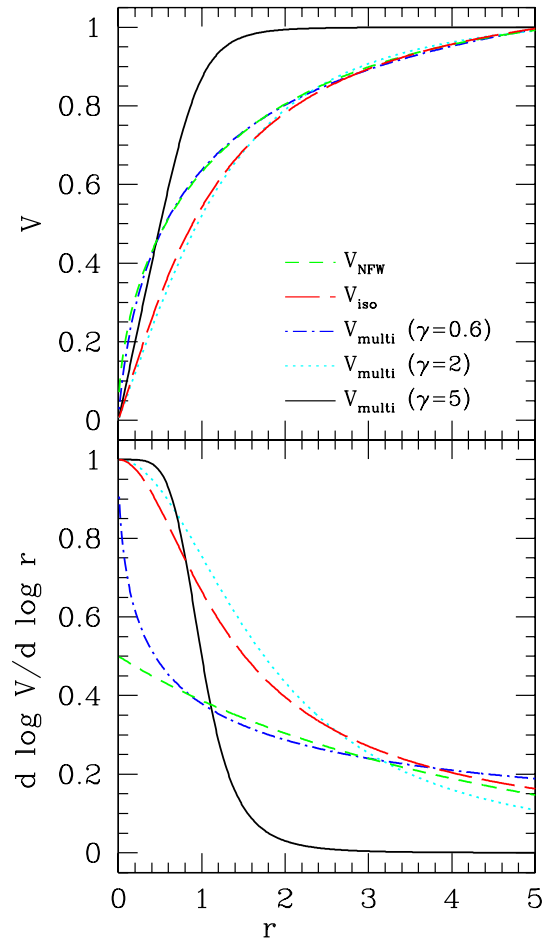
[10] See http://www.robswork.net/data.

Figure 6. Top panel: circular velocity profiles of NFW and pseudo-isothermal halo models along with the Courteau (1997) multiparameter fitting formula given by equation (7), plotted in arbitrary units of radius and velocity. The NFW profile has $(r_s, V_{max}) = (5.0, 1.0)$, the pseudo-isothermal profile has $(r_c, V_\infty) = (1.0, 1.2)$, and the multiparameter formula is shown for three different sets of parameters, $(r_t, \gamma, V_0) = (0.44, 0.6, 1.4)$, $(1.8, 2.0, 1.0)$ and $(1.0, 5.0, 1.0)$. Bottom panel: logarithmic slope of the velocity profiles. Equation (7) provides a good fit to both halo models despite the fact that, at small radii, it rises linearly with radius like the pseudo-isothermal velocity profile. Also, curves with $\gamma \lesssim 1$ turn over gently as a function of radius whereas those with $\gamma \gg 1$ rise linearly out to $r \simeq r_t$, then flatten sharply.

galaxies, the B02 sample consists of 26 LSB galaxies, and the S03 sample contains 10 dwarf galaxies and five LSB galaxies for a total of 67 galaxies in the total sample. Note that the raw Hα data were used, as opposed to the smoothed hybrid HI/Hα rotation curve data available for the M01 and B02 samples, in order to compile a data set with error characteristics as uniform as possible. Following the practice of S03, a minimum error of 5 km s^{-1} was imposed on the raw data from all three samples. Note that five galaxies – F568-3, UGC 731, UGC 4325, UGC 5750 and UGC 11557 – are common to two of the three data sets. We treat both versions of the rotation curve data independently for these galaxies, and below we note the good agreement between fits to them.

The top, middle and bottom rows of Figs 7 and 8 show a selection of rotation curves from the M01, B02 and S03 samples, respectively. For each rotation curve, a grid of χ^2 values is computed for fits obtained with equation (7). The solid curves in Figs 7 and 8 show

the best fit obtained for each rotation curve as determined by the minimum χ^2 value, subject to the following constraints:

$$r_t > 0$$
$$0 < \gamma \leqslant 5$$
$$V_0 \leqslant 2V_{max}.$$

The allowed range in γ was chosen because fits with $\gamma \gtrsim 5$ correspond to a virtually right-angle transition between the rising and flat parts of the curve. The limit on V_0 was chosen in order to avoid fits with asymptotic velocities much greater than the maximum indicated by the data. The reduced χ^2, χ^2_{red}, and fit parameter values are shown in Figs 7 and 8 under the column labelled 'min' for each rotation curve. The fit parameters for all 67 rotation curves are given in Table 2. The outermost radius with reliable data is listed as r_{outer}. For the five galaxies common to two of M01, B02 and S03, we find broad consistency between the two versions of the rotation curve data: in most of these, the best-fitting parameter values are within ~20 per cent of one another.

The top panel of Fig. 9 shows the distribution of best-fitting γ values obtained for each sample. Each histogram in this figure is normalized to the total number of systems in each sample for ease of comparison. All three rotation curve data sets are broadly consistent with each other; most (70 ± 5 per cent) of the rotation curves in each sample are characterized by a value of $\gamma \lesssim 2$. These are typically gently rising curves which turn over gradually as they approach the maximum asymptotic rotation speed, as shown by rotation curves in the left and middle columns of Fig. 7. A significant ($\simeq 30$ per cent) number of galaxies with $\gamma > 2$ are also present, however. These are galaxies whose rotation curves feature a linear rise in velocity with radius and a much sharper transition from the rising to flat part, as shown by many of the rotation curves in Fig. 8 and in the rightmost panels of Fig. 7.

5.3 Halo circular velocity profile shapes

The bottom panel of Fig. 9 shows the γ distribution obtained by fitting equation (7) to the V_c profile of all dwarf and galaxy-sized haloes. In order to consider various dynamical instances of a halo, we have included in the analysis about 20 different outputs for each system, spanning the redshift range $1 \lesssim z \leqslant 0$, giving a total of 266 halo profiles. At each redshift, we calculate the V_c profile at points separated by 1 kpc (physical) in radius for the galaxy haloes and 0.2 kpc (physical) in radius for the dwarf haloes, starting at the innermost reliably resolved radius r_{conv}. Because no formal error bars exist for the halo profiles (Poisson errors are negligible for the numbers of particles in these haloes), we assign a uniform error of ± 1 km s^{-1} to all points for the purpose of curve fitting. The V_c profiles were fit out to $r_{outer} = 20$ kpc (physical) for the galaxy haloes and $r_{outer} = 6$ kpc (physical) for the dwarf haloes, corresponding to 4–$5 r_d$, where r_d is the exponential scalelength of the discs embedded in such haloes, as predicted by the model of Mo, Mao & White (1998) (see below).

We note that the best-fitting parameter values are somewhat sensitive to the region fitted; for example, fitting the $z = 0$ V_c profile of halo G5 out to $r_{outer} = 10, 20, 40$ and 80 kpc results in best-fitting parameter values of $(r_t, \gamma, V_0) = (1.4$ kpc, 0.4, 363 km s$^{-1})$, $(1.6$ kpc, 0.5, 312 km s$^{-1})$, $(3.0$ kpc, 0.9, 220 km s$^{-1})$ and $(4.1$ kpc, 1.4, 198 km s$^{-1})$, respectively, whereas $(r_{max}, V_{max}) = (40.1$ kpc, 197 km s$^{-1})$ for this halo. The shape parameter γ therefore increases as a function of r_{outer}, but in general is limited to values of $\gamma \lesssim 1$ provided that $r_{outer} \lesssim r_{max}$, i.e. provided that fits do not extend beyond
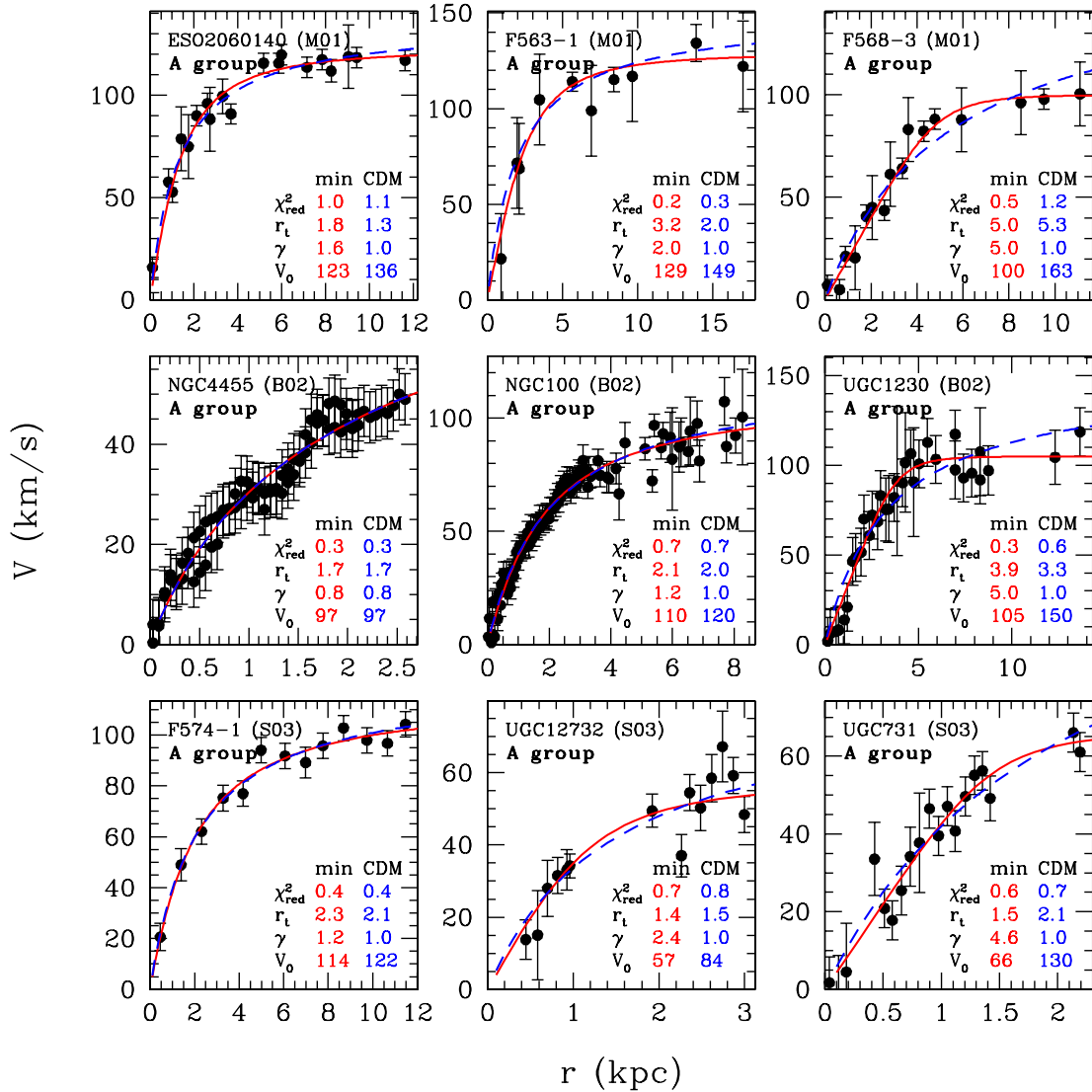
Figure 7. Hα rotation curves of LSB galaxies from the data sets of M01 (top row), B02 (middle row) and S03 (bottom row). Solid curves show best fits using the multiparameter fitting formula given by equation (7) with fit parameters and χ^2_{red} values listed under the 'min' column in each panel. Dashed curves show the best fits which can be obtained with ΛCDM-compatible parameters, listed under the 'CDM' column. In each row, rotation curves are ordered from left to right in order of increasing best-fitting γ values. All rotation curves in this figure belong to group A, defined as having ΛCDM-compatible fits with reasonable χ^2_{red} values ($\chi^2_{red} \leqslant 1.5$). See text for full discussion.

the radius at which it starts to decline. In addition, because velocity increases monotonically with radius in equation (7) (unlike halo V_c profiles which peak at a finite radius), the asymptotic velocity V_0 tends to overestimate V_{max}.

The γ distribution of all galaxy and dwarf haloes and that of the dwarf haloes alone are shown as the histograms normalized to the total number of haloes in the bottom panel of Fig. 6. The halo γ distribution peaks at $\gamma \simeq 0.6$, and has a dispersion of the order of ~0.4. For illustration, the three G1 V_c profiles shown in the bottom panel of Fig. 5 have $\gamma = 0.73$, 0.65 and 0.48 at $z = 1.1$, 0.48 and 0, respectively. There is no significant difference between the galaxy and dwarf halo γ distributions.

We note that the contribution of a baryonic component has not been taken into account in our analysis of the simulated V_c profiles. In order to assess the effect of a baryonic disc on the shape of the V_c profile, we construct an analytical mass model comprised of an NFW halo and an exponential disc. We use the prescription of

Mo et al. (1998) to determine the scalelength of the disc, r_d, as a function of the concentration, $c = r_{200}/r_s$, and spin parameter, λ, of the NFW halo, and the mass, m_d, and angular momentum, j_d, of the disc (expressed as fractions of the halo mass and angular momentum, respectively). Fig. 10 shows the inner V_c profiles of the disc and halo components along with best fits using equation (7).

The V_c profile of a dwarf NFW halo with $r_{200} = 50\,h^{-1}$ kpc and concentration $c = 13.7$, as predicted by the Bullock et al. (2001) concentration model, fit over the range $r_{min} = 0.2$ kpc to $r_{outer} = 6.0$ kpc is best fit by a curve with $\gamma = 0.59$. The addition of a disc with $m_d = j_d = 0.05$ to a halo with $\lambda = 0.1$ (as expected for LSB galaxies), results in best fits with $\gamma = 0.64$ for the halo after adiabatic contraction ($V_{NFW,adia}$), and $\gamma = 0.66$ for the total circular velocity, $V^2_{tot} = V^2_{disc} + V^2_{NFW,adia}$. Note that this choice of parameters for the size and mass of the disc yields a central surface brightness of 22.5 mag arcsec^{-2}, assuming $\Upsilon_B = 2$ for the *B*-band stellar mass-to-light ratio, similar or slightly brighter than that of a
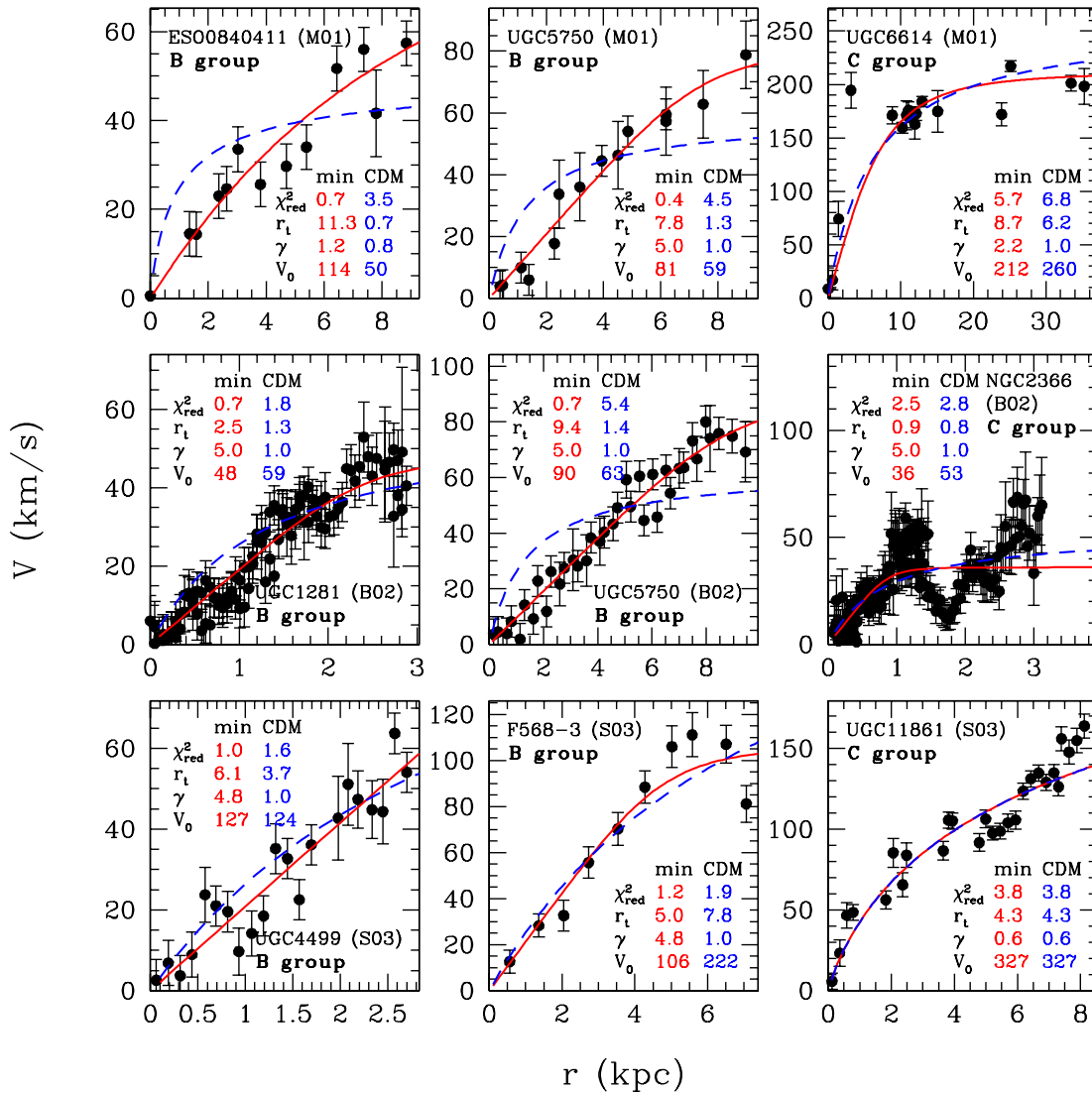
Figure 8. Same as Fig. 8 but featuring all six rotation curves from group B and three from group C. Rotation curves from group B are those for which a good fit with ΛCDM-compatible parameters cannot be found. The best fits for these rotation curves typically have high values of γ, corresponding to a linear rise in velocity with radius and, in some cases, a sharp transition from the rising to the flat part of the curve. Galaxies in group C have irregular rotation curves for which simple fitting functions such as equation (7) cannot provide a good fit. See text for full discussion.

typical LSB galaxy. We therefore conclude that, for reasonable LSB disc parameters, the increase in γ due to the presence of the disc is small.

Taken at face value, the halo γ distribution in Fig. 9 appears to be inconsistent with that of LSB galaxies. Most haloes have $\gamma < 1$ compared to only about one-third of LSBs. However, the rotation curve data have error estimates associated with each of the velocities, whereas the halo V_c profiles have negligible statistical errors. One should take this into account in order to decide whether the shapes of LSB rotation curves are consistent with simulated halo V_c profiles. In Section 5.5 we address this issue in detail, identifying galaxies that are inconsistent with the structure of CDM haloes even after taking the observational uncertainties into consideration.

5.4 Concentration of LSB haloes

The discussion of the preceding section focused on the shape of the rotation curves and halo V_c profiles. We now turn our attention to the

physical parameters of the fits, in order to address claims that LSB galaxies are surrounded by haloes of much lower concentration than expected in the ΛCDM scenario (McGaugh & de Blok 1998; de Blok et al. 2001b). We emphasize again that it is important to characterize both the observational data and the simulations in a way that is as independent as possible from fitting formulae or extrapolation. Alam, Bullock & Weinberg (2002) recently proposed a simple and useful dimensionless measure of central density that satisfies these criteria:

$$\Delta_{V/2} \equiv \frac{\overline{\rho}(r_{V/2})}{\rho_{\rm crit}}. \tag{9}$$

The central density parameter, $\Delta_{V/2}$, measures the mean density contrast (relative to the critical density for closure) within the radius $r_{V/2}$ at which the rotation speed drops to one-half of its maximum value, $V_{\rm max}$. In practice, we estimate $\bar{\rho}(r)$ by $3\,V_c^2(r)/4\pi Gr^2$, a quantity that is easily measured both in galaxies with rotation curve data (and well-defined $V_{\rm max}$) and in simulated haloes. To be precise,

we shall adopt $r_{V/2} = r_t/(2^\gamma - 1)^{1/\gamma}$ as the radius where the velocity equals one-half of its asymptotic value V_0.

The top panel of Fig. 11 shows $\Delta_{V/2}$ as a function of V_{max} for all simulated haloes. The open and solid symbols show the 'true' $\Delta_{V/2}$ values calculated directly from the V_c profiles of the dwarf and galaxy-sized haloes, respectively. The starred and skeletal symbols show the $\Delta_{V/2}$ values estimated from fits to the V_c profiles. This

figure illustrates the uncertainty in the central densities and maximum velocities inferred from fits to rotation curve data. Recall that halo V_c profiles are fit out $r_{outer} \lesssim 0.5\, r_{max}$ in most cases, and, as a result, V_0 overestimates the true V_{max} of the halo by up to 60 per cent in some cases. This implies that values of $\Delta_{V/2}$ estimated from fits to the halo profiles can underestimate the true central density parameter by up to a factor of 5.

Table 2. Properties of rotation curves and fit parameters.

Galaxy ID	r_{max} (kpc)	V_{max} (km s^{-1})	r_{outer} (kpc)	r_t (kpc)	γ	V_0 (km s^{-1})	$\log \Delta_{V/2}$	$\chi^2_{red,min}$	$\chi^2_{red,CDM}$
M01:									
ESO0140040	11.5	300.2	29.2	0.9	0.4	509	5.0	3.0	3.0
ESO0840411	8.8	57.4	8.8	11.3	1.2	114	4.2	0.7	3.5
ESO1200211	3.2	30.1	3.5	1.1	5.0	23	5.2	0.4	0.7
ESO1870510	2.1	41.2	3.0	1.4	0.8	71	5.1	0.3	0.3
ESO2060140	6.0	119.8	11.6	1.8	1.6	123	6.1	1.0	1.1
ESO3020120	10.9	91.5	10.9	3.1	1.8	91	5.4	0.3	0.3
ESO3050090	2.8	76.9	4.7	2.8	5.0	57	5.2	2.2	2.8
ESO4250180	8.8	175.2	14.2	5.5	0.6	314	4.6	1.2	1.2
ESO4880049	6.0	101.0	6.0	3.5	0.8	181	5.1	0.7	0.7
F563-1	13.9	134.2	17.0	3.2	2.0	129	5.7	0.2	0.3
F568-3	11.1	100.4	11.1	5.0	5.0	100	5.2	0.5	1.2
F571-8	10.0	140.1	10.0	2.8	0.6	261	5.0	0.8	0.8
F579-V1	9.9	167.0	11.5	1.1	1.2	127	6.3	1.9	1.9
F583-1	6.3	82.1	7.2	3.7	2.0	88	5.2	0.5	0.7
F583-4	6.7	70.6	6.7	1.8	0.6	128	4.8	1.2	1.3
F730-V1	13.3	156.3	14.8	2.3	1.4	151	5.9	0.5	0.6
UGC4115	0.9	40.4	1.0	1.1	1.2	74	5.9	0.5	0.6
UGC5750	9.0	78.8	9.0	7.8	5.0	81	4.6	0.4	4.5
UGC6614	25.1	217.1	35.3	8.7	2.2	212	5.3	5.7	6.8
UGC11454	10.5	153.1	12.2	2.7	1.2	173	5.8	1.1	1.1
UGC11557	6.2	83.4	6.2	8.2	1.4	149	4.8	1.9	3.3
UGC11583	1.5	38.7	1.5	0.9	5.0	35	5.8	0.3	0.4
UGC11616	9.3	151.4	9.6	2.3	1.6	143	6.0	0.6	0.7
UGC11648	12.7	142.7	12.7	0.8	0.4	277	4.6	2.1	2.2
UGC11748	6.0	264.6	21.0	2.3	5.0	242	6.6	7.2	40.4
UGC11819	8.4	157.4	11.6	4.4	1.8	178	5.7	0.7	0.9
B02:									
DDO47	1.4	65.6	1.5	1.6	0.7	119	5.2	0.3	0.3
DDO52	0.7	40.6	0.8	2.1	5.0	78	5.7	1.0	1.3
DDO64	2.1	50.9	2.1	2.2	1.0	100	5.3	0.4	0.4
DDO185	2.2	57.4	2.2	5.9	5.0	114	5.2	0.5	0.9
DDO189	3.8	84.2	3.8	5.3	0.8	168	4.7	1.2	1.2
IC2233	6.5	95.7	7.4	3.9	0.6	191	4.4	2.0	2.3
F563-1	9.3	108.5	9.7	1.3	0.6	147	5.2	0.3	0.3
NGC100	7.7	107.3	8.3	2.1	1.2	110	5.6	0.7	0.7
NGC1560	4.4	82.7	4.7	2.3	0.6	156	4.7	1.7	1.7
NGC2366	2.8	68.7	3.1	0.9	5.0	36	5.8	2.5	2.8
NGC3274	2.4	86.3	2.5	0.4	0.6	134	6.1	0.7	0.7
NGC4395	5.0	95.9	5.2	1.2	0.6	143	5.2	0.8	0.8
NGC4455	2.5	50.0	2.6	1.7	0.8	97	5.2	0.3	0.3
NGC5023	3.6	90.6	4.1	1.6	0.8	144	5.6	1.2	1.2
UGC628	13.8	141.4	13.8	1.8	1.2	130	5.9	0.7	0.8
UGC711	15.4	110.0	15.4	7.3	1.2	128	4.7	1.8	3.6
UGC731	4.9	73.7	5.0	1.3	3.8	71	6.1	0.5	0.7
UGC1230	13.6	118.7	13.6	3.9	5.0	105	5.5	0.3	0.6
UGC1281	2.4	52.9	2.9	2.5	5.0	48	5.2	0.7	1.8
UGC3137	5.0	154.7	5.4	2.3	5.0	102	5.9	0.4	0.6
UGC3371	5.1	73.8	6.1	3.5	2.6	69	5.1	0.5	0.6
UGC4173	0.8	20.5	2.5	0.1	3.2	12	6.7	0.1	0.1
UGC4325	4.6	128.8	4.6	3.0	3.6	114	5.7	0.9	0.9
UGC5005	8.1	66.2	10.4	2.5	5.0	56	5.3	0.3	0.3
UGC5750	8.0	80.0	9.4	9.4	5.0	90	4.6	0.7	5.4
UGC10310	3.9	78.1	5.2	5.5	2.0	104	5.0	0.4	0.5

Table 2 – *continued*

Galaxy ID	r_{max} (kpc)	V_{max} (km s^{-1})	r_{outer} (kpc)	r_t (kpc)	γ	V_0 (km s^{-1})	$\log \Delta_{V/2}$	$\chi^2_{red,min}$	$\chi^2_{red,CDM}$
S03:									
F563-V2	7.5	113.1	7.5	2.5	4.8	113	5.9	0.04	1.2
F568-1	8.6	130.1	8.6	2.6	1.0	169	5.6	0.3	0.3
F568-3	5.6	111.2	7.1	5.0	4.8	106	5.3	1.2	1.9
F568-V1	8.9	124.9	8.9	2.2	1.2	135	5.8	0.6	0.7
F574-1	11.5	104.2	11.5	2.3	1.2	114	5.6	0.4	0.4
UGC731	2.1	66.1	2.2	1.5	4.6	66	5.9	0.6	0.7
UGC2259	1.7	93.7	2.8	0.8	2.0	83	6.5	1.7	1.8
UGC4325	2.8	104.6	2.8	2.8	1.0	191	5.7	0.5	0.5
UGC4499	2.6	63.7	2.7	6.1	4.8	127	5.2	1.0	1.6
UGC5721	2.2	80.4	2.4	0.4	0.6	126	6.0	0.4	0.4
UGC8490	1.3	74.0	1.3	1.6	1.0	141	5.9	0.8	0.8
UGC11557	6.8	80.1	6.8	5.6	0.8	160	4.6	0.5	1.1
UGC11707	2.9	62.3	3.0	1.3	0.8	102	5.5	0.3	0.3
UGC11861	8.1	164.0	8.1	4.3	0.6	327	4.8	3.8	3.8
UGC12732	2.7	67.2	3.0	1.4	2.4	57	5.8	0.7	0.8
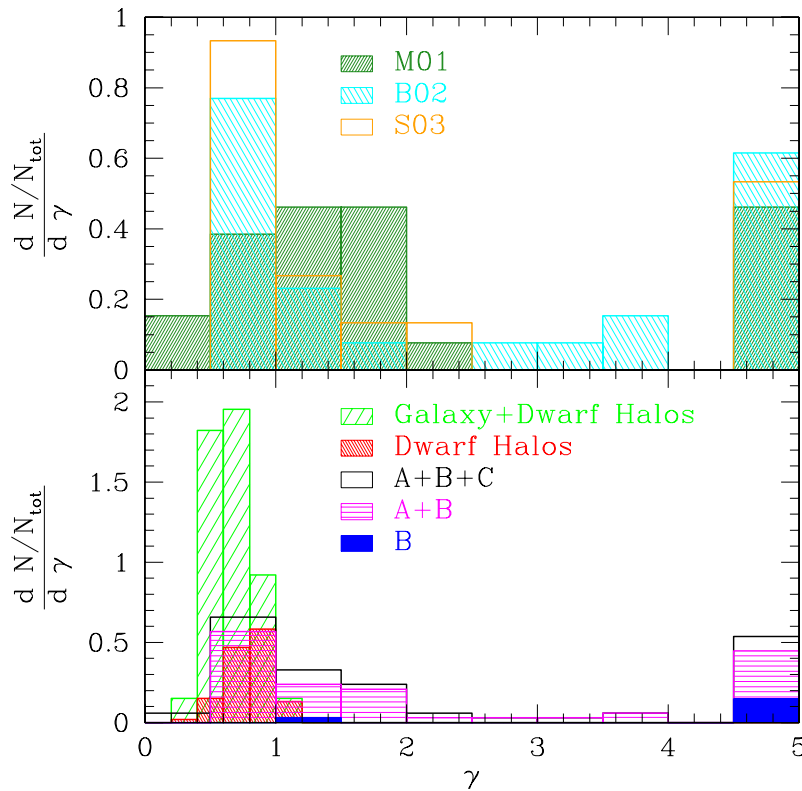
Figure 9. Top panel: distribution of best-fitting γ values obtained for galaxies in the samples of M01, B02 and S03. All three data sets are roughly consistent with one another and about 70 per cent of the rotation curves in each sample have $\gamma \lesssim 2$. Bottom panel: halo and LSB γ distributions. LSB data are sorted by χ^2 groups, as defined in Fig. 12. All simulated haloes have $\gamma \lesssim 1$, whereas many LSBs have $\gamma > 1$. However, most LSBs are members of group A, shown by the horizontally hatched region of the histogram, and have acceptable fits with $\gamma \leqslant 1$. Group B members, shown by the solid region of the histogram, have γ values and/or central densities that are inconsistent with those of haloes. Group C members, shown by the open region of the histogram, are not well fit by simple functions such as equation (7).

The solid curves in all panels of Fig. 11 correspond to the predictions of the Eke, Navarro & Steinmetz (2001) halo concentration model for NFW haloes in the ΛCDM cosmology assumed in our simulations.[11] The dotted curves show the predictions of the Bullock

et al. (2001) concentration model, together with the 1σ halo-to-halo scatter predicted by their model.[12]

---

[11] A code which calculates this model is made available by the authors at http://pinot.phys.uvic.ca/~jfn/cens/.

[12] A code which calculates this model is made available by the authors at http://cfa-www.harvard.edu/~jbullock/WWW/CVIR/. Note that this code implements the correct 1σ halo-to-halo scatter for this model, $\Delta(\log c_{vir}) = 0.14$, as opposed to the erroneous value $\Delta(\log c_{vir}) = 0.18$ reported in the
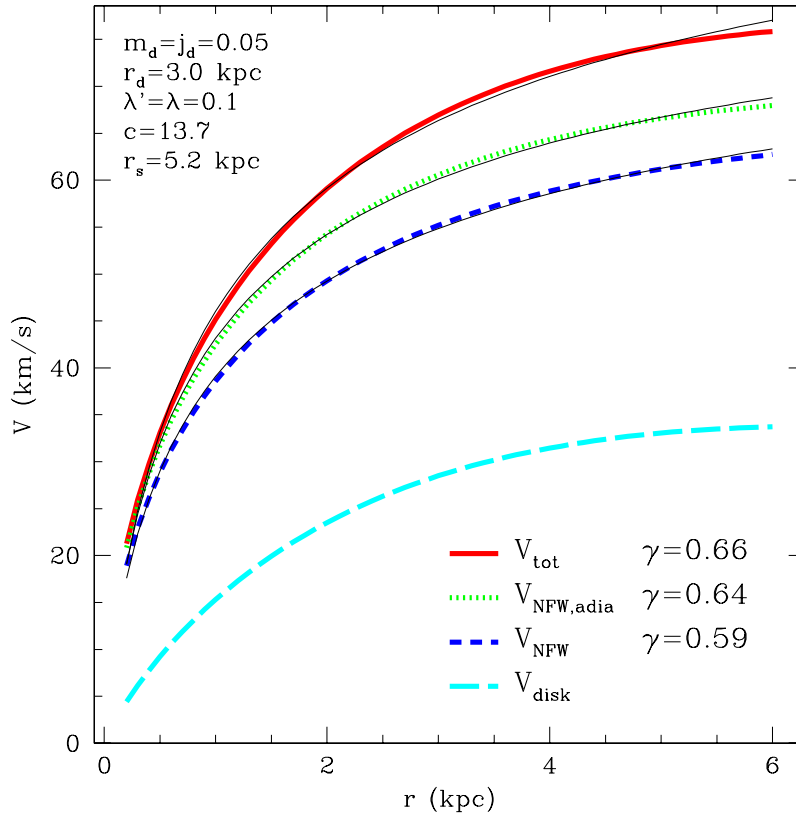
Figure 10. Circular velocity profiles of a disc galaxy modelled according to the prescription of Mo et al. (1998). Parameters of the galaxy model are shown at the top left, where m_d and j_d are the mass and angular momentum of the disc (in units of the corresponding quantities for the halo), r_d is the exponential scalelength of the disc, λ and λ' are the spin parameters of the disc and halo, respectively, r_s is the scalelength of the NFW halo, and $c = r_{200}/r_s$ is the halo concentration parameter. Thick lines show the V_c profiles of the disc (V_{disc}), the NFW halo (V_{NFW}), the halo after adiabatic contraction ($V_{NFW,adia}$), and the total velocity $V_{tot}^2 = V_{disc}^2 + V_{NFW,adia}^2$. Best fits to the V_c profiles with equation (7) are shown as thin solid lines. The addition of an LSB disc results in only a small change in the best-fitting value of γ, from $\gamma = 0.59$ for the NFW halo to $\gamma = 0.66$ for V_{tot}.

The middle panel of Fig. 11 shows that the 'true' central densities of the simulated dwarf, galaxy and cluster haloes in our sample (skeletal symbols) are in rough agreement with both models; the Bullock et al. (2001) model reproduces the central densities of simulated haloes slightly better on the scales of dwarf haloes, whilst the Eke et al. (2001) model does better on the scale of clusters. This figure also shows the estimated central densities of all galaxies in the M01, B02 and S03 samples (open symbols). We find that a large fraction of galaxies in the LSB sample lie below the ΛCDM predictions of the simulated haloes and the concentration models. Based on this apparent excess of low-concentration galaxies, Zentner & Bullock (2002) have argued for substantial revision of the 'concordance' ΛCDM scenario, such as tilted power spectra, running spectral index, or perhaps a lower σ_8. However, as previously noted, V_{max} and $\Delta_{V/2}$ are not well defined for some LSBs, and may bias the halo central density parameter estimates inferred from rotation curve data. We explore this issue in detail in the following section.

5.5 Identifying galaxies inconsistent with ΛCDM haloes

We now attempt to identify rotation curves that are of sufficient quality to provide meaningful constraints on the structure of dark matter haloes. A glance at the rotation curves shown in Figs 7 and 8

text (but not the figures) of Bullock et al. (2001). For further details, see Wechsler et al. (2002).

indicates that uncertainties in the data allow for a variety of acceptable fit parameters. In order to identify galaxies that are robustly discrepant with the predictions of ΛCDM cosmologies, we search the grid of χ_{red}^2 values for the best fit which satisfies the following constraints:

$$r_t > 0$$

$$0 < \gamma \leqslant 1$$

$$V_0 \leqslant 2V_{max}$$

$$|\log \Delta_{V/2} - \log \Delta_{V/2,CDM}| \leqslant 0.7,$$

i.e. with γ limited to the range found for simulated haloes and central densities within a factor of 5 of the value predicted for ΛCDM haloes. Here we take the median prediction of the Bullock et al. (2001) model for a halo with V_{max} equal to the fit V_0 as the fiducial value $\Delta_{V/2,CDM}$. We note that this model predicts a 1σ scatter of $\Delta \log \Delta_{V/2} \simeq 0.4$. However, we choose a more generous range of 0.7 to allow for uncertainties in the predictions of the model, as shown by the haloes which fall outside the 1σ limits on $\Delta_{V/2}$ in Fig. 11.

In Fig. 12 we plot $\chi_{red,min}^2$, the reduced χ^2 value found for the best fit, against $\chi_{red,CDM}^2$, the minimum value found for fits subject to these additional constraints. Plotted in this way, the data fall into three broad categories:

(A) rotation curves that are well fit by equation (7) and for which a good fit with ΛCDM-compatible parameters can also be found, i.e. $\chi_{red,min}^2 \leqslant 1.5$ and $\chi_{red,CDM}^2 \leqslant 1.5$;
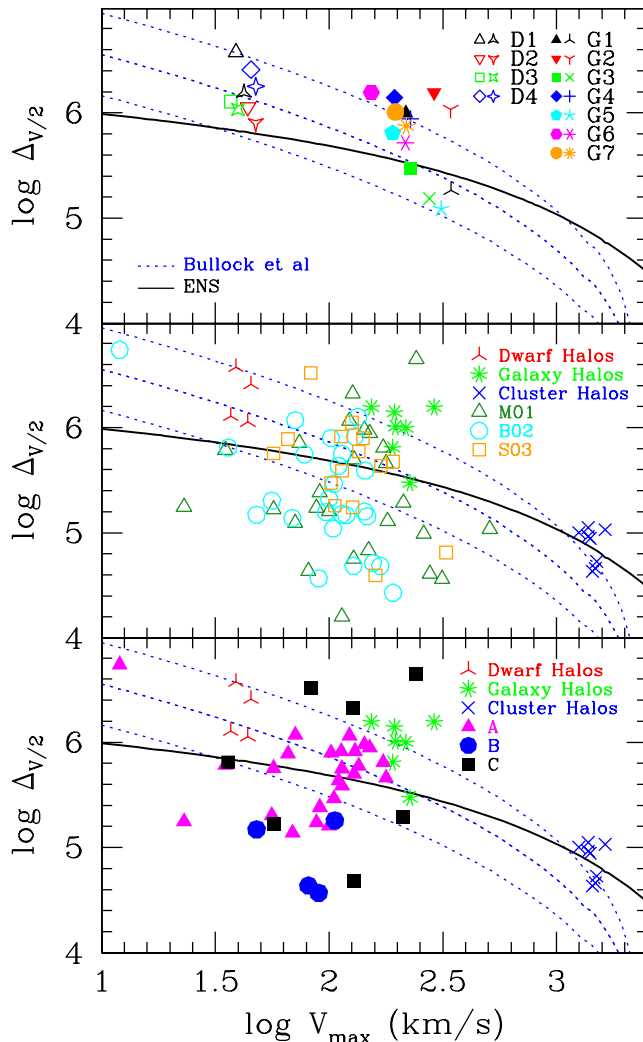
Figure 11. Top panel: Alam et al. (2002) halo central density parameter, $\Delta_{V/2}$, for simulated dwarf and galaxy-sized haloes versus maximum velocity V_{max}. Solid and open symbols show $\Delta_{V/2}$ and V_{max} values measured directly from V_c profiles; skeletal and starred symbols show $\Delta_{V/2}$ and V_{max} values estimated from fits to V_c profiles with equation (7), taking the asymptotic velocity of the fit, V_0, as the estimate of V_{max}. The solid line shows the prediction of the Eke et al. (2001) concentration model for NFW haloes in a ΛCDM cosmogony ($\Omega_0 = 0.3$, $\Omega_\Lambda = 0.7$ and $h = 0.65$, $\sigma_8 = 0.9$). Dotted lines show the prediction (and 1σ scatter) corresponding to the Bullock et al. (2001) concentration model. Middle panel: central densities of simulated dwarf, galaxy and cluster-sized haloes calculated directly from their V_c profiles (skeletal symbols) compared with $\Delta_{V/2}$ and $V_{max}(=V_0)$ values calculated from fits to LSB rotation curves from M01, B02 and S03 data sets (open symbols). Lower panel: same as middle panel, but with LSB $\Delta_{V/2}$ values sorted by χ^2 groups shown in Fig. 12. Only galaxies with well-defined maximum velocities are shown.

(B) rotation curves that are well fit by equation (7) but for which no good fit with ΛCDM-compatible parameters can be found, i.e. $\chi^2_{red,min} \leqslant 1.5$ and $\chi^2_{red,CDM} > 1.5$;

(C) rotation curves that are poorly fit by equation (7), i.e. $\chi^2_{red,min} > 1.5$ and $\chi^2_{red,CDM} > 1.5$; these are rotation curves that do not rise smoothly and monotonically with radius, and for which no simple fitting function provides a good fit.

The choice of $\chi^2_{red} \leqslant 1.5$ as the criterion for a good fit is somewhat arbitrary, but leads to a natural grouping of the data points in Fig. 12,

shown by the regions bounded by solid lines and labelled 'A', 'B' and 'C'. The number of galaxies in each of these regions is 48, 7 and 12 for groups A, B and C, respectively. The rotation curves shown in Fig. 7 belong to group A, whereas those shown in Fig. 8 are members of groups B and C, as identified by the labels below the name of each galaxy.

We use solid symbols in Fig. 12 to denote rotation curves for which the asymptotic velocity of the best fit is no more than 20 per cent greater than the maximum velocity observed in the data, i.e. $V_0 < 1.2 V_{max}$. These galaxies, which represent about half of the total sample, have maximum velocities that are reasonably well defined by their rotation curves. Galaxies with $V_0 \geqslant 1.2 V_{max}$, represented by open symbols, typically have rotation curves that are still rising at their outermost radius and consequently have poorly constrained fit parameters and $\Delta_{V/2}$ values. In fact, most of these galaxies have best fits with $V_0 = 2 V_{max}$, the maximum asymptotic velocity permitted by our fitting criteria. In these cases, the rotation curve data resolve only the rising part of the circular velocity profile and are clearly insufficient to constrain the structure and maximum circular velocity of the dark matter halo of the corresponding galaxy. Examples of these include NGC 4455 in Fig. 7, and ESO 0840411, UGC 4499 and UGC 11861 in Fig. 8.

In summary, galaxies in group A are consistent with ΛCDM in terms of their inferred central densities and the shape of their rotation curves; galaxies in group B are inconsistent with ΛCDM; and galaxies in group C have irregular rotation curves for which fitting functions such as equation (7) do not provide a good fit. Of the six rotation curves in group B which pose a problem for ΛCDM, only four of these have best fits with asymptotic velocities within 20 per cent of the maximum observed rotation velocity.

The bottom panel of Fig. 9 shows the γ distribution of rotation curves in each of the three groups. The open histogram represents the distribution of the entire sample, the horizontal hatched portion shows the contribution of LSBs from groups A and B, and the solid portion shows the contribution of group B only. It is clear from this panel that most of the rotation curves that are best fit by $\gamma > 1$ are actually members of group A, for which a reasonable $\gamma \leqslant 1$ fit (consistent with CDM) exists. In fact, the majority of rotation curves with $\gamma \simeq 5$ belong to group A. The rightmost column of Fig. 7 shows three examples of these. The rotation curves of these galaxies do not vary smoothly as a function of radius and some contain points with rather large error bars. As a result, these data, although best fit by a curve with an abrupt change in slope (high γ), can also be well fit with a more gently flattening curve (lower γ) by compensating with a different value of V_0.

Most of the galaxies in group B have $\gamma \simeq 5$; however, the case for a high-γ fit is hardly unambiguous in the raw data. In most cases, the data cut off before the flat part of the curve is well resolved, and the fits are driven to high values of γ because this allows for a positive velocity gradient in the outer regions, not because the data show a sharp transition between a rising part and a flat part. This is corroborated by the fact that $r_t \gtrsim r_{outer}$ even for the four galaxies with $V_0 < 1.2 V_{max}$, illustrating that our criterion for rotation curves having well-defined maximum velocities is somewhat lenient. In summary, the group B galaxies with high γ have rotation curves which sample only the rising parts of these curves; therefore, it is difficult to determine the overall shapes of these curves.

We also note that the rotation curve of galaxy F568-3 derived by S03 (see Fig. 8) is a member of group B; however, the M01 rotation curve of the same galaxy (see Fig. 7) belongs to group A. The M01 data do extend out 20 per cent further than the S03 data,
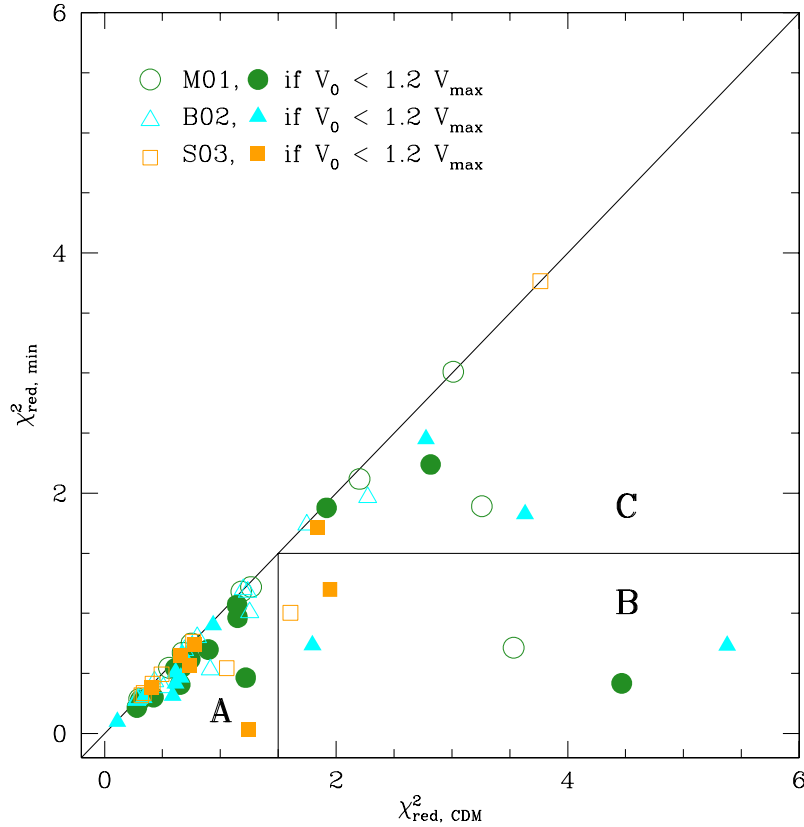
Figure 12. Reduced χ^2 values of best fits to rotation curves from M01, B02 and S03 data sets versus χ^2 values of best fits with ΛCDM-compatible parameters. Solid (open) symbols represent rotation curves with best-fitting values of V_0 within 20 per cent of (more than 20 per cent greater than) their maximum velocities, V_{max}. Data fall into three groups: (A) galaxies that are consistent ($\chi^2 < 1.5$) with ΛCDM in terms of the shapes of their rotation curves and their inferred central densities; (B) galaxies that are inconsistent with ΛCDM; (C) galaxies with irregular rotation curves for which simple fitting functions such as equation (7) do not provide a good fit.

but the best-fitting parameter values for these two rotation curves are nearly identical and both have $\gamma \simeq 5$. The error estimates on the S03 velocities are significantly smaller however, resulting in $\chi^2_{red,CDM} > 1.5$ for the best ΛCDM-compatible fit to the S03 rotation curve. This illustrates the sensitivity of the χ^2 statistic to error estimates and also underlines the somewhat arbitrary nature of the $\chi^2_{red} \leqslant 1.5$ criterion for a good fit.

We show the central densities of the LSB galaxies identified by membership in A, B and C groups in the bottom panel of Fig. 11. Only points with well determined V_{max}, i.e. $V_0 < V_{max}$, are shown as solid symbols in this plot. Note that galaxies with poorly constrained maximum velocities may have best-fitting values of V_0 that underestimate or overestimate the true maximum velocity of the galaxy, because the fit is essentially an extrapolation of data which samples only the rising part of the rotation curve. As noted by Alam et al. (2002), errors in the determination of V_{max} and $r_{V/2}$ have cancelling effects if the rotation curve is linear near $r_{V/2}$. However, this may not be the case for galaxies such as NGC 4455 shown in Fig. 7. Estimates of $\Delta_{V/2}$ based on fits to halo V_c profiles out to radii smaller than r_{max} can underestimate the true central density by up to a factor of 5. Therefore, it is perhaps not surprising that many of the LSB points which lie below the ΛCDM predictions in the middle panel of Fig. 11 correspond to galaxies whose rotation curves do not extend out far enough to resolve their maximum velocities and are thus excluded from the bottom panel.

As in the bottom panel of Fig. 9, the $\Delta_{V/2}$ values inferred from best fits to rotation curves in group A cannot be considered to be ro-

bustly inconsistent with ΛCDM because acceptable fits with values of $\Delta_{V/2}$ within a factor of 5 of the theoretical predictions can be obtained for these galaxies. The $\Delta_{V/2}$ values of group C galaxies with well-defined V_{max} cannot be dismissed out of hand, because some rotation curves with 'noisy' data have reasonably well-determined $r_{V/2}$ radii, despite having relatively large χ^2_{red} values. In any event, these galaxies, represented by the solid squares in the bottom panel of Fig. 11, appear to be evenly scattered above and below the predictions of the Bullock et al. model.

Of the group B galaxies, the maximum velocity, and therefore $\Delta_{V/2}$, is uncertain for most, if not all, of them. On the other hand, if we assume that our estimates of $\Delta_{V/2}$ are robust for galaxies with $V_0 < 1.2 V_{max}$, we are faced with galaxies that have roughly the same V_{max}, but central densities that vary by almost two orders of magnitude.

As previously noted, Zentner & Bullock (2002) have argued for substantial revision of the ΛCDM scenario based on the low-concentration galaxies in LSB samples. It appears unlikely, however, that any such modification to the 'concordance' cosmology would result in the larger range of central densities suggested by the data. It is unclear at this point how to reduce the disagreement, but any resolution to the puzzle must explain why so many LSBs are actually consistent with ΛCDM haloes and why any disagreement is confined to a minority of systems. The possibility remains that some complex astrophysical process not yet considered in the models might actually be behind the discrepancy and that no radical modification to the ΛCDM paradigm is called for.

In summary, we find that the shapes of the rotation curves and the inferred central densities of most galaxies that appear inconsistent with the predictions of ΛCDM are, in fact, insufficiently constrained by the data. Of the 67 galaxies in the entire data set, a ΛCDM-compatible fit can be found for 48 of these, and an additional 12 have rotation curves that cannot be well fit by any smoothly varying function, such as equation (7). The rotation curves of the remaining six galaxies are characterized by a linear rise in velocity with radius; however, many of these do not extend out far enough to accurately determine their shapes and central densities. We conclude that, within the limitations of the observational data, this sample of LSB rotation curves is not manifestly inconsistent with the predictions of ΛCDM cosmological models.

6 CONCLUSIONS

We present results from a set of high-resolution cosmological simulations of dark matter haloes formed in a ΛCDM cosmogony. Seven MW-sized galaxy haloes were simulated at various mass, time and spatial resolutions, enabling us to investigate the convergence properties of cosmological *N*-body simulations. We have examined the internal structure of the highest-resolution realization of each halo, with particular emphasis on the logarithmic slope of the inner density profile. Finally, we have compared the circular velocity profiles of these haloes and of additional dwarf galaxy haloes with the observed rotation curves of a large sample of dwarf and LSB galaxies.

Our main conclusions may be summarized as follows.

(i) The convergence criteria proposed by P03 are robust, and provide a conservative estimate of the minimum radius at which the circular velocity profile of simulated haloes can be reliably predicted (to within 10 per cent). According to these criteria, the highest-resolution galaxy haloes we have simulated (which contain two to four million particles within the virial radius) are reliably resolved down to $r_{\rm conv} \simeq 1\, h^{-1}$ kpc.

(ii) The slope of ΛCDM halo density profiles becomes progressively shallower all the way down to the minimum reliably resolved radius, with little sign of convergence to a well-defined power law near the centre.

(iii) In general, the slope changes with radius more gradually than predicted by the NFW formula, which leads some haloes to be better described by profiles with steeper cusps, such as the modification to the NFW formula proposed by M99. There is, however, significant variation from halo to halo in the radial dependence of the slope. Some systems are better fit by the NFW profile, and others by the M99 formula. At $r_{\rm conv}$, however, all the density profiles are significantly shallower than $r^{-1.5}$, the asymptotic value advocated by M99.

(iv) A comparison of the circular velocity profiles of CDM haloes with rotation curves of LSB galaxies indicates that the shapes of the rotation curves and the inferred central densities of most (about 70 per cent) LSB galaxies are consistent with those of simulated haloes within the limitations imposed by observational error. Of the remainder, 20 per cent have irregular rotation curves which cannot be fit by simple fitting functions, and 10 per cent are inconsistent with CDM haloes.

We conclude that the inner structure of ΛCDM haloes is not manifestly inconsistent with the majority of LSB rotation curves. Although some rotation curves feature a sharp transition from the rising to the flat part of the curve, most of these can also accommodate a fit that is compatible with the shapes of CDM halo $V_{\rm c}$ profiles. A small minority of rotation curves exhibit a linear rise in velocity over a substantial range in radius that appears inconsistent with the shapes of halo $V_{\rm c}$ profiles. The data also suggest that the central densities of galaxies inferred from their rotation curves may exhibit a larger variation than is predicted for ΛCDM haloes.

We note, however, that the analysis presented in this paper is based on the assumption that the gas rotation speed is directly proportional to the spherically averaged halo circular velocity, an assumption which may not be valid for real galaxies. CDM haloes, for example, are known to be triaxial, which may lead gaseous discs to deviate systematically and significantly from simple coplanar circular orbits. Work is in progress to try and determine whether such asymmetries in the potential are able to account quantitatively for the observed variety of LSB rotation curves and concentrations.

REFERENCES

Alam S. M. K., Bullock J. S., Weinberg D. H., 2002, ApJ, 572, 34
Barnes J., Efstathiou G., 1987, ApJ, 319, 575
Blais-Ouellette S., Amram P., Carignan C., 2001, AJ, 121, 1952
Bullock J. S., Kolatt T. S., Sigad Y., Somerville R. S., Kravtsov A. V., Klypin A. A., Primack J. R., Dekel A., 2001, MNRAS, 321, 559
Burkert A., 1995, ApJ, 447, L25
Côté S., Carignan C., Freeman K. C., 2000, AJ, 120, 3027
Courteau S., 1997, AJ, 114, 2402
Crone M. M., Evrard A. E., Richstone D. O., 1994, ApJ, 434, 402
Davis M., Efstathiou G., Frenk C. S., White S. D. M., 1985, ApJ, 292, 371
de Blok W. J. G., Bosma A., 2002, A&A, 385, 816 (B02)
de Blok W. J. G., McGaugh S. S., Bosma A., Rubin V. C., 2001a, ApJ, 552, L23
de Blok W. J. G., McGaugh S. S., Rubin V. C., 2001b, AJ, 122, 2396
Dubinski J., Carlberg R. G., 1991, ApJ, 378, 496
Eke V. R., Navarro J. F., Steinmetz M., 2001, ApJ, 554, 114
Fillmore J. A., Goldreich P., 1984, ApJ, 281, 1
Flores R. A., Primack J. R., 1994, ApJ, 427, L1
Frenk C. S., White S. D. M., Efstathiou G., Davis M., 1985, Nat, 317, 595
Frenk C. S., White S. D. M., Davis M., Efstathiou G., 1988, ApJ, 327, 507
Fukushige T., Makino J., 1997, ApJ, 477, L9
Fukushige T., Makino J., 2001, ApJ, 557, 533
Fukushige T., Kawai A., Makino J., 2004, ApJ, 606, 625
Ghigna S., Moore B., Governato F., Lake G., Quinn T., Stadel J., 2000, ApJ, 544, 616
Gunn J. E., Gott J. R. I., 1972, ApJ, 176, 1
Hoffman Y., Shaham J., 1985, ApJ, 297, 16
Jimenez R., Verde L., Oh S. P., 2003, MNRAS, 339, 243
Jing Y. P., Suto Y., 2002, ApJ, 574, 538
Jing Y. P., Mo H. J., Borner G., Fang L. Z., 1995, MNRAS, 276, 417
Klypin A., Kravtsov A. V., Bullock J. S., Primack J. R., 2001, ApJ, 554, 903
McGaugh S. S., de Blok W. J. G., 1998, ApJ, 499, 41

McGaugh S. S., Rubin V. C., de Blok W. J. G., 2001, AJ, 122, 2381 (M01)

Mo H. J., Mao S., White S. D. M., 1998, MNRAS, 295, 319

Moore B., 1994, Nat, 370, 629

Moore B., Governato F., Quinn T., Stadel J., Lake G., 1998, ApJ, 499, L5

Moore B., Ghigna S., Governato F., Lake G., Quinn T., Stadel J., Tozzi P., 1999, ApJ, 524, L19 (M99)

Navarro J. F., 2003, in Makino J., Hut P., eds, Proc. IAU Symp. 208, Astrophysical SuperComputing using Particles. Kluwer, Dordrecht

Navarro J. F., Frenk C. S., White S. D. M., 1995, MNRAS, 275, 720

Navarro J. F., Frenk C. S., White S. D. M., 1996, ApJ, 462, 563

Navarro J. F., Frenk C. S., White S. D. M., 1997, ApJ, 490, 493

Navarro J. F. et al., 2004, MNRAS, 349, 1039

Power C., Navarro J. F., Jenkins A., Frenk C. S., White S. D. M., Springel V., Stadel J., Quinn T., 2003, MNRAS, 338, 14 (P03)

Quinn P. J., Salmon J. K., Zurek W. H., 1986, Nat, 322, 329

Spergel D. N., Steinhardt P. J., 2000, Phys. Rev. Lett., 84, 3760

Springel V., Yoshida N., White S. D. M., 2001, NewA, 6, 79

Stadel J. G., 2001, PhD thesis, University of Washington

Stoehr F., White S. D. M., Springel V., Tormen G., Yoshida N., 2003, MNRAS, 345, 1313

Swaters R. A., Madore B. F., Trewhella M., 2000, ApJ, 531, L107

Swaters R. A., Madore B. F., van den Bosch F. C., Balcells M., 2003, ApJ, 583, 732 (S03)

Taylor J. E., Navarro J. F., 2001, ApJ, 563, 483

Thomas P. A. et al., 1998, MNRAS, 296, 1061

van den Bosch F. C., Swaters R. A., 2001, MNRAS, 325, 1017

van den Bosch F. C., Robertson B. E., Dalcanton J. J., de Blok W. J. G., 2000, AJ, 119, 1579

Warren M. S., Quinn P. J., Salmon J. K., Zurek W. H., 1992, ApJ, 399, 405

Wechsler R. H., Bullock J. S., Primack J. R., Kravtsov A. V., Dekel A., 2002, ApJ, 568, 52

White S. D. M., Zaritsky D., 1992, ApJ, 394, 1

Zentner A. R., Bullock J. S., 2002, Phys. Rev. D, 66, 43003

This paper has been typeset from a T_EX/L^AT_EX file prepared by the author.